

Prediction of Hardness and Residual Stress in Orthogonal Cutting of Inconel 718

Yisi Liu

A Thesis

in

The Department

of

Mechanical, Industrial and Aerospace Engineering

Presented in Partial Fulfillment of the Requirements

for the Degree of

Master of Applied Science (Mechanical Engineering) at

Concordia University

Montreal, Quebec, Canada

April 2021

© Yisi Liu, 2021

CONCORDIA UNIVERSITY

School of Graduate Studies

This is to certify that the thesis prepared

By: **Yisi Liu**

Entitled: **Prediction of Hardness and Residual Stress in Orthogonal Cutting of Inconel 718**

and submitted in partial fulfillment of the requirements for the degree of Master of

Master of Applied Science

complies with the regulations of the University and meets the accepted standards with respect to originality and quality.

Signed by the final Examining Committee:

_____ Chair
Dr. Y. Zhang

_____ Examiner
Dr. L. Wang

_____ Examiner
Dr. Y. Zhang

_____ Supervisor
Dr. Z. C. Chen

Approved by _____ Chair of Department or Graduate Program Director
Dr. Mamoun Medraj

_____ Dean of Faculty
Dr. Mourad Debbabi

Date _____
May 6, 2021

ABSTRACT

Prediction of Hardness and Residual Stress in Orthogonal Cutting of Inconel 718

Yisi Liu

Due to its high strength in high temperatures, Inconel 718 is widely used in the aerospace industry. However, Inconel 718 is a difficult-to-cut alloy with poor machinability. For instance, the cutting force is high in cutting Inconel 718, resulting in work-hardening of the machined surface and high residual stress in the machined surface. When residual stress releases, the part deforms and scrapes with error beyond tolerance. Therefore, it is necessary to predict the residual stress in the machined surface under a set of machining conditions. By modifying the machining conditions, the residual stress in the machined surface is under control, and the part deformation is limited. In this research, an analytical approach to the hardness and the residual stress in the machined surface in orthogonal cutting is proposed. This research has advantages over the experiment, the conventional approach and the FEA methods. With this approach, the cutting parameters can be optimized to minimize the residual stress in the machined surface and improve the surface integrity.

ACKNOWLEDGEMENTS

Firstly I would like to express my deepest gratitude to my supervisor, Dr. Chevy Chen, for his inspiring instruction and suggestions on my thesis. He spent a lot of time reading my drafts and gave a lot of valuable advice. When we encounter academic difficulties, he always does his best to support us. His remarkable academic reputation has always inspired me.

I would also like to thank all my fellows for their help and encouragement over the past three years. They gave me inspiration and advice in my research.

Finally, I want to express my gratitude to my parents, thanks for their support and love.

TABLE OF CONTENTS

List of Figures	VIII
List of Tables	XII
CHAPTER 1 INTRODUCTION	1
1.1 Background.....	1
1.2 Work hardening and residual stress in Inconel 718 machining	6
1.2.1 Inconel 718 properties.....	7
1.2.2 Work-hardening in Inconel 718 machining	9
1.2.3 Residual stress in Inconel 718 machining	11
1.3 Literature review	12
1.4 Research problems and objectives	15
1.5 Thesis outline	16
CHAPTER 2 STRESS MODELING IN ORTHOGONAL CUTTING	17
2.1 Cutting force in orthogonal cutting.....	17
2.1.1 Cutting force prediction theory	19
2.1.2 Cutting force measurement.....	26

2.2	Stress modeling in orthogonal cutting	28
CHAPTER 3 HARDNESS AND RESIDUAL STRESS MODELING		37
3.1	Material yield and work-hardening.....	37
3.1.1	Material yield criterion	37
3.1.2	Work-hardening.....	38
3.2	Hardness modeling.....	40
3.2.1	Hardness measurement.....	40
3.2.2	Hardness modeling in orthogonal cutting	41
3.3	Residual stress in machining	43
3.4	Residual stress modeling in orthogonal cutting.....	46
CHAPTER 4 VERIFICATION AND APPLICATION.....		49
4.1	Verification with the orthogonal cutting of AISI 316L	49
4.1.1	Introduction to a conventional experiment of cutting AISI 316L	49
4.1.2	Application of this proposed method to AISI 316L.....	53
4.2	Application of the purposed method to Inconel 718.....	56
4.2.1	Cutting parameters optimization with the software	56
4.2.2	Application of cutting parameters optimization	57

CHAPTER 5 CONCLUSIONS AND FUTURE WORK	62
5.1 Conclusions.....	62
5.2 Future work.....	62
BIBLIOGRAPHY	64

List of Figures

Figure 1.1 A schematic of a cutaway of the turbofan engine.....	2
Figure 1.2 Temperature and pressure profiles for Rolls-Royce Trent 800 which powers Boeing 777	2
Figure 1.3 Materials used for Rolls-Royce Trent 800.....	3
Figure 1.4 Stress rupture resistance of different alloys.....	4
Figure 1.5 Continuous chips and high temperature in the milling of Inconel 718	5
Figure 1.6 Flat machined airframe component distorted due to residual stress.....	6
Figure 1.7 Six components of surface Integrity	7
Figure 1.8 High-temperature tensile properties of Inconel 718 bar with a diameter of 13 mm after hot rolling, annealing and ageing	9
Figure 1.9 Stress-strain curve of a simple uniaxial tensile test.....	10
Figure 1.10 Micrograph of the surface in the feed direction	11
Figure 1.11 Mechanical–thermal contact in 2D orthogonal machining [25].....	11
Figure 2.1 Cutting forces in orthogonal turning	17
Figure 2.2 Micrograph of the partially formed chip of metal cutting	18

Figure 2.3 Cutting force modeling of orthogonal cutting	19
Figure 2.4 Chip formation model used in the analysis [42]	20
Figure 2.5 Flow chart of cutting force prediction model	25
Figure 2.6 Cutting force dynamometer in a turning machine	26
Figure 2.7 The measuring principle of the piezoelectric sensor	27
Figure 2.8 Measurement system for cutting force in turning	28
Figure 2.9 Contact stress history	29
Figure 2.10 Contact model of boundary loads	30
Figure 2.11 Stress components in the coordinate frame of the shear plane.....	31
Figure 2.12 Stress components in the coordinate frame of the cutting edge contact area	32
Figure 2.13 Geometric relationship of the coordinate frames.....	32
Figure 2.14 Stress state for the arbitrary point in the material layer at a certain depth	35
Figure 2.15 Simplified flow chart for the algorithm of the stress	36
Figure 3.1 Yield surface in the stress space	38
Figure 3.2 Stress-strain curve of the work-hardened material	39

Figure 3.3 Dislocations and their motions [58].....	40
Figure 3.4 Steel indenter forced on the surface in the hardness test.....	41
Figure 3.5 Work hardening and hardness.....	42
Figure 3.6 Residual macro stress (type I) and residual micro stress in grain scale (type II or intergranular stresses) [63]	44
Figure 3.7 Schematic diagram of the generation of residual stress in machining proposed by Jacobus.....	45
Figure 3.8 Work hardening in the first machining and second machining.....	46
Figure 4.1 Stress history by Huang et al. ($Z=3\mu\text{m}$) [25]	51
Figure 4.2 von Mises stress field by Huang et al. [25]	52
Figure 4.3 Comparison of residual stress [25]	52
Figure 4.4 Stress history by the improved method ($Z=3\mu\text{m}$).....	53
Figure 4.5 von Mises stress field by the improved method	54
Figure 4.6 Comparison of residual stress.....	55
Figure 4.7 Residual stress of the surface layer	55
Figure 4.8 Prediction software.....	56
Figure 4.9 Cutting parameters optimization.....	57

Figure 4.10 Residual stress of set 1.....	59
Figure 4.11 Residual stress of set 2.....	59
Figure 4.12 Microhardness of set 1	60
Figure 4.13 Microhardness of set 2	61

List of Tables

Table 1.1 The main features of Inconel 718 machining	4
Table 1.2 Chemical Composition of Inconel 718, %.....	8
Table 1.3 Properties of Inconel 718.....	8
Table 4.1 Properties of AISI 316 L.....	49
Table 4.2 AISI 316L cutting conditions.....	50
Table 4.3 Cutting conditions and measured variables for Inconel 718.....	58

CHAPTER 1 INTRODUCTION

1.1 Background

Aero-engine is vital to aircraft. When an engine is running, the air is ingested by a large and spinning fan and is squeezed by a compressor in gradually reduced space [1]. The air pressure and its energy potential are increased. The compressed air is mixed with the fuel and is ignited in the combustor, and then the temperature inside the combustor could reach 1500°C or more. The hot air with high pressure flows into the turbine blades and rotates the blades to empower the compressor, when the air exits the nozzle, it generates the thrust for the aircraft to fly. Figure 1.1 shows the structure of a turbine engine [2]. Some aero-engine parts, such as the turbine blades, serve more than 10000 hours of flying (or 8 million km of flight) at a temperature of over 1000 °C, thus, they must be able to withstand high temperatures and pressure [3]. Furthermore, the turbine spins at a speed of several thousand to tens of thousands of revolutions per minute, which means that the speed of the blade tip can reach 1200 km/h and stress at the blade root can reach 180 MPa (or 20 tsi). Figure 1.2 shows an engine structure and its temperature and pressure profiles [4]. It can be found that the pressure could reach 40 standard atmospheres, and the temperature could be more than 1400°C.

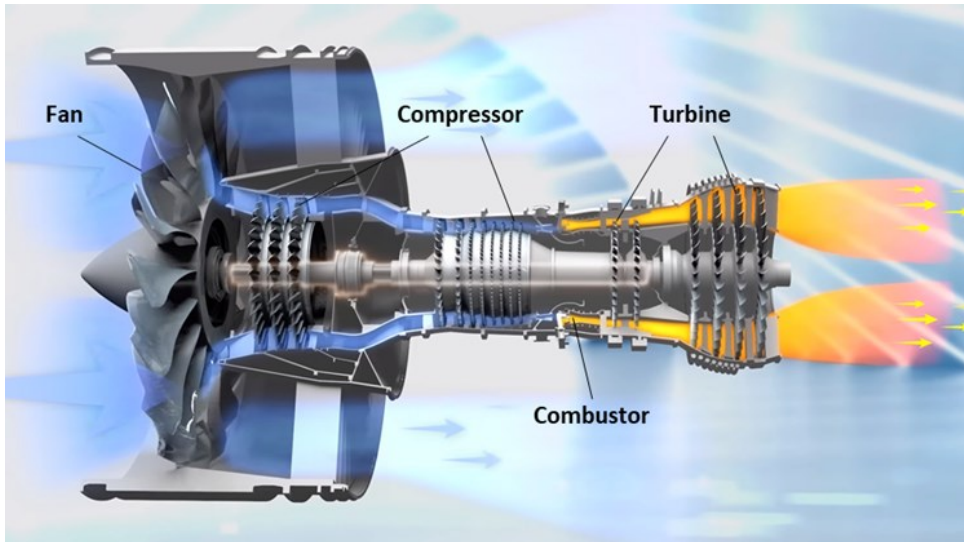


Figure 1.1 A schematic of a cutaway of the turbofan engine

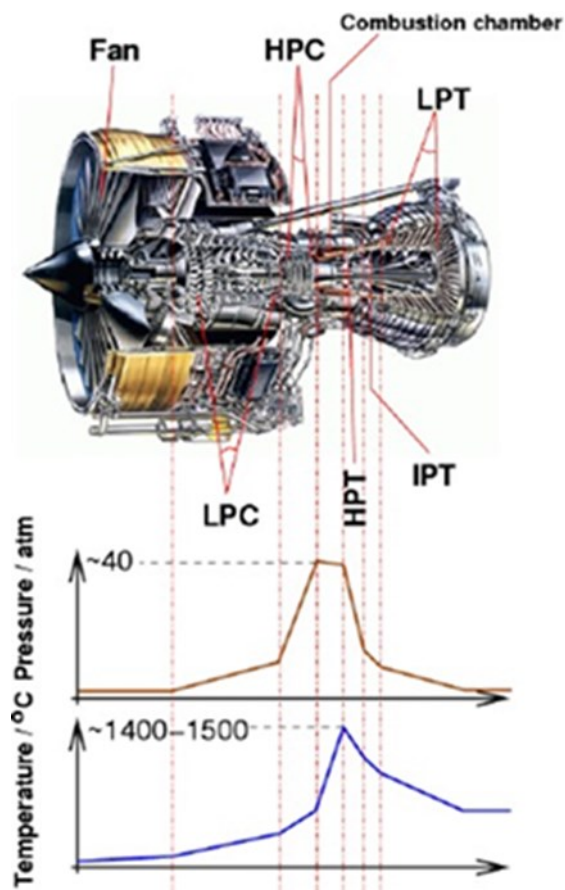


Figure 1.2 Temperature and pressure profiles for Rolls-Royce Trent 800 which powers Boeing 777

Nickel-based superalloy, e.g., Inconel 718, is widely employed in the aerospace industry. Figure 1.3 shows the materials applied for the Rolls-Royce Trent 800 [5]. Nickel-based superalloy is used in the combustion chamber, turbine and turbine casing. Not only has nickel-based superalloy a high melting point, but also has considerable resistance to mechanical degradation for a long time. Most other materials rapidly creep at the temperature of about 35% of their melting temperatures [3]. For example, titanium alloy creeps at 350 °C, and aluminum alloy at 150 °C. The creep resistance of nickel-based alloy exceeds those of other metals, and the rapid creep temperature of nickel-based alloy exceeds its melting point by 50%. The final stage of creep failure is stress rupture. Compared to other metals, the nickel-based alloy has outstanding stress rupture resistance, which is shown in Figure 1.4. The above comparison means that nickel-based superalloy is less likely to distort and crack under high temperature and pressure than other materials. Besides that, many properties of nickel-based superalloys, such as high strength, long fatigue life, corrosion and oxidation resistance at high temperatures, are suitable for the aero-engine material.

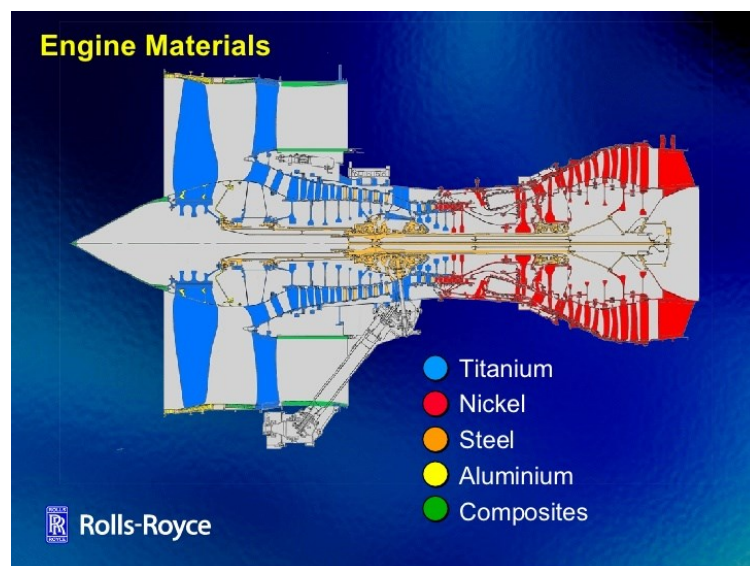


Figure 1.3 Materials used for Rolls-Royce Trent 800

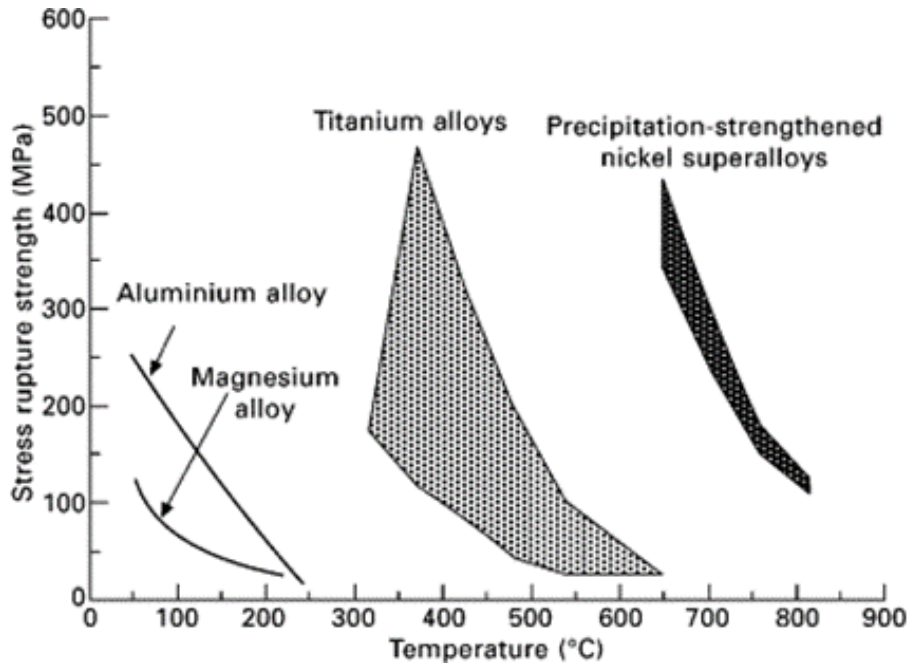


Figure 1.4 Stress rupture resistance of different alloys

However, nickel-based superalloy has been recognized as one of the most difficult to cut alloys. Table 1.1 shows the main features in machining Inconel 718.

Table 1.1 The main features of Inconel 718 machining

Cutting force	The atomic structure of nickel-based alloy is very stable. A lot of energy is required to destroy the atomic balance resulting in greater cutting force [6].
Cutting temperature	The lower thermal conductivity is only about 30% of general steel, which will cause a large amount of heat to be unable to diffuse and accumulate in the cutting area and the cutting tool (Figure 1.5). The cutting temperature can even reach 1,300°C [7].
Tool wear	Hard abrasive carbides in the alloy lead to high abrasive wear, and the increase in temperature during the cutting process will also cause a chemical reaction between the tool and the metal resulting in an increased wear rate.[8]

Chip control The chips produced during the machining process are more difficult to break (Figure 1.5 [9]) especially when the cutting speed is low, which results in the performance decrease of the cutting tool.[10]



Figure 1.5 Continuous chips and high temperature in the milling of Inconel 718

Due to the high-quality requirements for aero-engine components, the aero-engine industry has focused on machining Inconel 718. Inconel 718 has high strength at high temperatures and low thermal conductivity; thus, work hardening could occur in machining [11][12]. Work hardening of Inconel 718 has a significant negative influence on the integrity of the machined surface and causes severe tool wear [13][14]. Therefore, work hardening is a non-negligible factor affecting the engine part cutting efficiency and fatigue life.

Another problem in machining Inconel 718 is the residual stress generated on the machined surface. When residual stress is released, the machined surface deformed and its dimension is changed. For example, residual stress on thin-walled parts can result in part distortion and part out-of-tolerance. Figure 1.6 in [15] shows a distorted airframe component. Residual stress also negatively affects part performance [16]. Some properties of the machined surface, especially fatigue life,

are greatly affected by residual stress [17]. Usually, residual tensile stress is uncondusive to the fatigue life of mechanical parts. Engine turbines work under high cyclic loads, the residual tensile stress is fatal to the engine turbines [18]. Besides, residual tensile stress aggravates micro-crack propagation, and excessive surface cracks fail parts.



Figure 1.6 Flat machined airframe component distorted due to residual stress

1.2 Work hardening and residual stress in Inconel 718 machining

Surface integrity mainly includes two aspects: (1) topography, texture, and surface finish, and (2) metallurgy, hardness, and residual stress. Figure 1.7 in [19] shows the six groups of key factors in surface integrity definition. Excellent characteristics of Inconel 718 make it widely used in the aero-engine. However, Inconel 718 has a high strain hardening rate and a high possibility of residual stress. In machining, the material undergoes plastic deformation and becomes chips. The top layer of the machined surface is then work-hardened, and the yield strength and hardness of the work-hardened material are changed. The inhomogeneous plastic deformation of Inconel 718 causes large residual stress. In the following, the properties of Inconel 718 and the basics of residual stress and work hardening are

introduced.

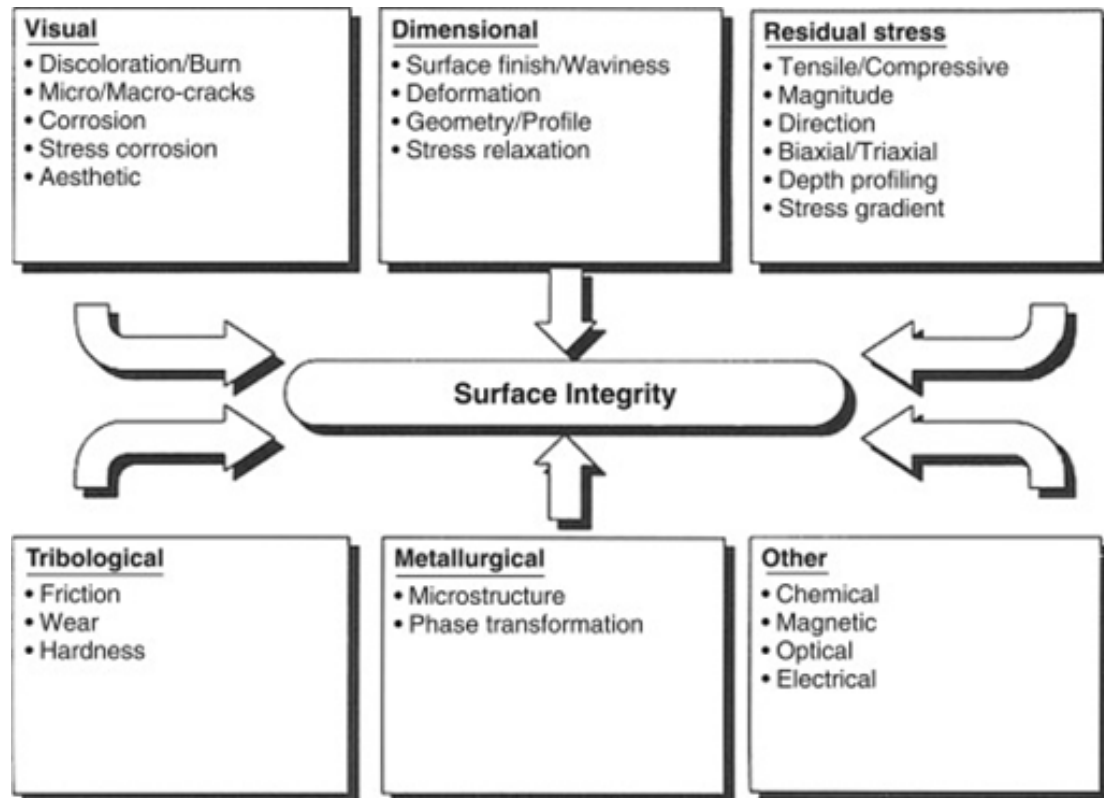


Figure 1.7 Six components of surface Integrity

1.2.1 Inconel 718 properties

Inconel 718 is a Ni-Fe-Cr superalloy, also known as a high-temperature alloy. Since Special Metal Co. invented Inconel 718 in the last century [20], Inconel 718 has become the most extensively used nickel-based superalloy in the history of aero-engine manufacturing. Table 1.2 and Table 1.3 [21] show the main chemical composition and main properties of Inconel 718, respectively. This material is often used for age-hardenable alloys and complex parts. It has excellent weldability and post-weld cracking resistance. It has superior strength at high temperatures, and the creep resistance of nickel alloys exceeds that of most metals [3]. Figure 1.8 [21] shows the high-temperature tensile properties of Inconel 718.

Table 1.2 Chemical Composition of Inconel 718, %

Nickel (plus Cobalt)	50.00-55.00
Chromium	17.00-21.00
Iron	17
Niobium (plus Tantalum)	4.75-5.50
Molybdenum	2.80-3.30
Titanium	0.65-1.15
Aluminum	0.20-0.80
Cobalt	1.00 max.
Carbon	0.08 max.
Manganese	0.35 max.
Silicon	0.35 max.
Phosphorus	0.015 max.
Sulfur	0.015 max.
Boron	0.006 max.
Copper	0.30 max.

Table 1.3 Properties of Inconel 718

Density	8.19 g/cc
Tensile Strength, Ultimate (20°C)	1375 MPa
Tensile Strength, Ultimate (650°C)	1100 MPa
Tensile Strength, Yield (20°C)	1100 MPa
Tensile Strength, Yield (650°C)	980 MPa
Elongation (20°C)	25%
Elongation (650°C)	18%
Coefficient of Linear Thermal Expansion (20°C)	13 $\mu\text{m}/\text{m}\cdot^\circ\text{C}$

Specific Heat Capacity	0.435 J/g·°C
Thermal Conductivity	11.4 W/m·K
Melting Point	1260 - 1336 °C

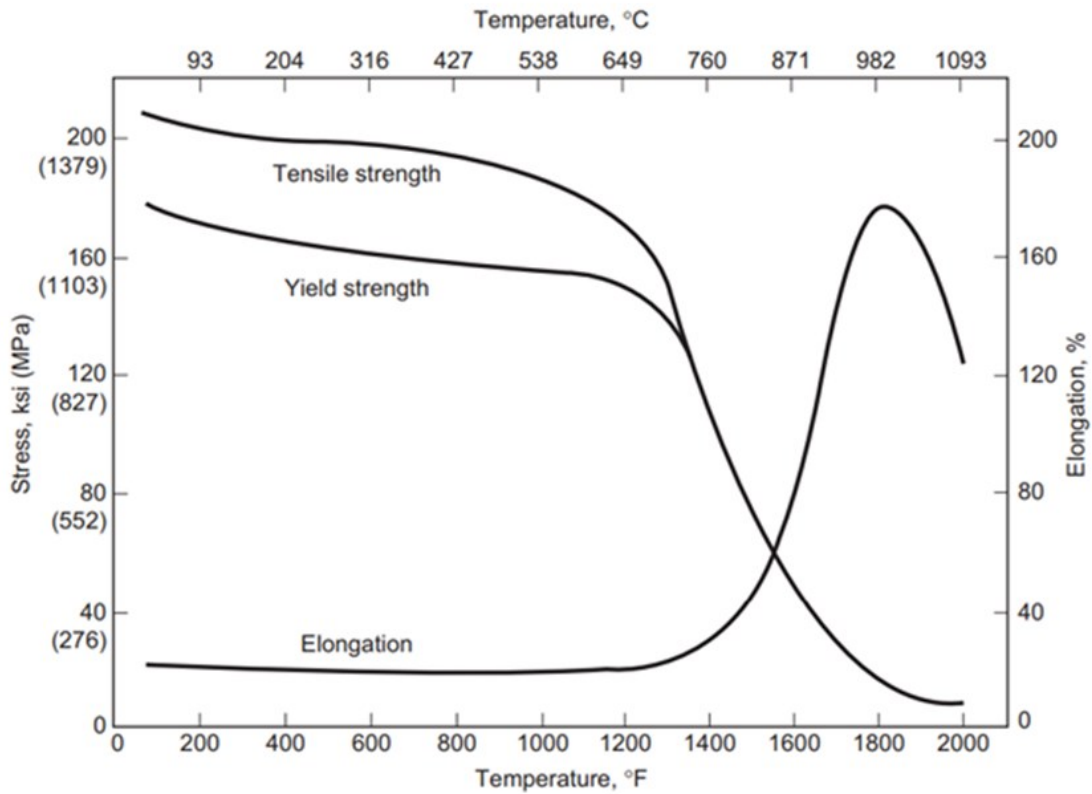


Figure 1.8 High-temperature tensile properties of Inconel 718 bar with a diameter of 13 mm after hot rolling, annealing and ageing

1.2.2 Work-hardening in Inconel 718 machining

The increase in strength and hardness when the material undergoes plastic deformation is called work hardening. For example, in the metal uniaxial tensile test, the specimen experiences work hardening. Figure 1.9 shows the stress-strain curve of a simple uniaxial tensile test [22]. The material first undergoes elastic deformation and then plastic deformation. The yield point B is the critical point from the elastic

deformation state to the plastic deformation state. In the stage of elastic deformation, and the relationship between stress and strain is linear. In the stage of plastic deformation, if the stress decreases, the material unloads in an elastic mode along the path CD, which is parallel to AB. When the material is loaded again, the material loads along DC and its yield point and corresponding yield strength changes. If the yield strength becomes larger, the material is work-hardened.

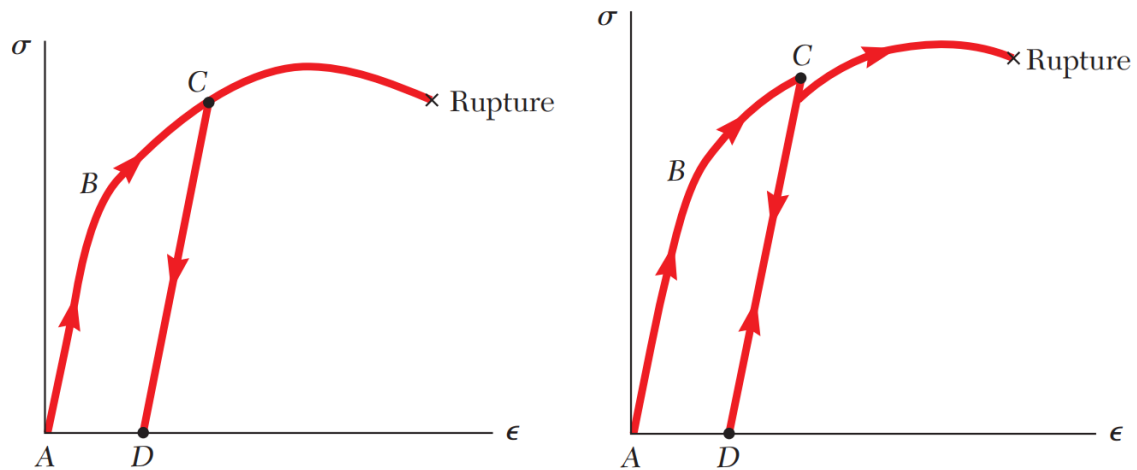


Figure 1.9 Stress-strain curve of a simple uniaxial tensile test

A large cutting force is required to cut Inconel 718 for its high strength. The pressure between the tool and the workpiece is high, and the material in the cutting area is in severe plastic deformation. The dislocation and the grain refinement in the deformed material generate work hardening. Besides, due to the high temperature in cutting and low thermal conductivity of Inconel 718, a large amount of heat in cutting accumulates in the cutting area, causing the austenite matrix of the nickel-based alloy to precipitate and work hardening [23]. Figure 1.10 [24] shows the micrograph of a work-hardening layer. Work hardening strengthens the material and retards further machining. The hardness of the machined surface increases, which causes severe tool wear.

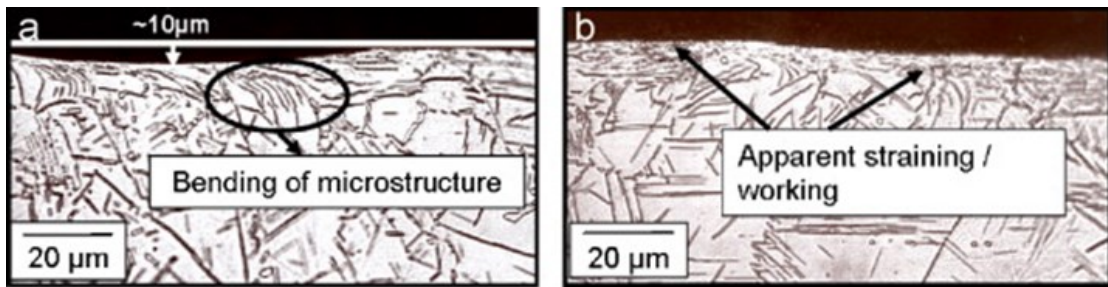


Figure 1.10 Micrograph of the surface in the feed direction

1.2.3 Residual stress in Inconel 718 machining

Residual stresses are stresses that remain on the part surface after machining. Cutting Inconel 718 generates residual stresses on the surface and the subsurface of the machined components. Residual stress exists inside the part without external force or moment. The deformation is different at different depths of the machined surface. Inhomogeneous deformation throughout the workpiece section is the reason for residual stress.

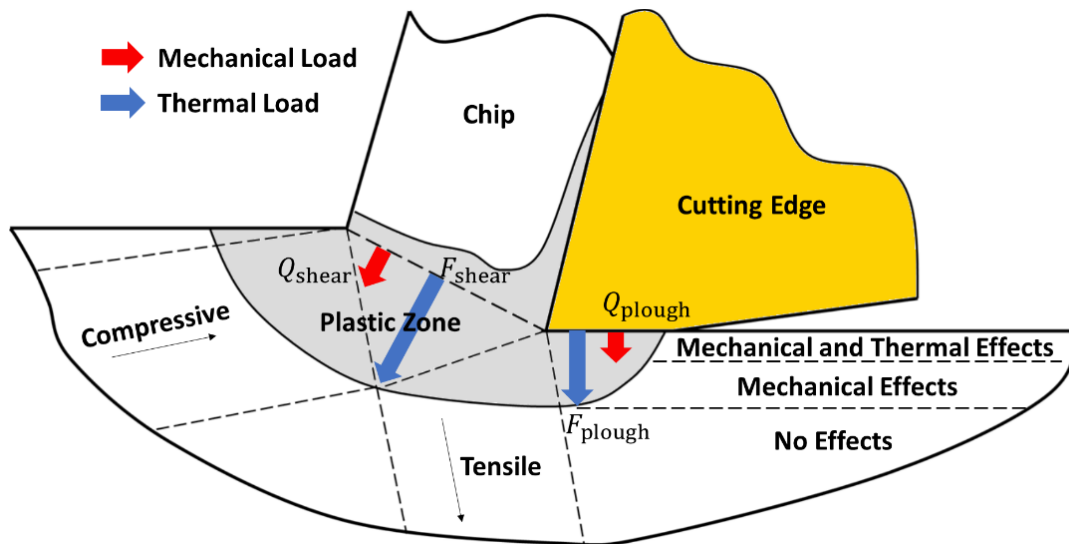


Figure 1.11 Mechanical–thermal contact in 2D orthogonal machining [25]

In the cutting process, stressed material in the plastic zone is generated shown in Figure 1.11. When the tool is fed forward, the material moves into the stress area

and undergoes compressive plastic deformation, which is tensioned in the direction perpendicular to the cutting direction. The friction and ploughing of the tool flank wear also cause plastic deformation on the machined surface. On the other hand, a lot of heat is generated during the cutting process. Due to the poor thermal conductivity of Inconel 718, this heat accumulates in the cutting area, resulting in material deformation. In the stable orthogonal cutting process, materials in different depths experience different degrees of mechanical and thermal effects and different yields and plastic deformation. The microstructure of Inconel 718 is permanently displaced in plastic deformation, and the thermal gradient changes the volume of the material. This inhomogeneous elastoplastic deformation generates residual stresses in the workpiece.

1.3 Literature review

Since Inconel 718 is highly sensitive to work hardening, and work-hardened materials have significant effects on machining, many studies about the work hardening in Inconel machining have been presented. Coelho et al. [26] reported that the hardness of the machined surface is higher than that of the bulk material, and the compressed layer is caused by hardening during the machining process. Zhuang et al. [27] analyzed the impact of notch wear on the work hardening layer in Inconel 718 turning and built a model to predict the notch wear. Sharman et al. [28] presented that the microhardness and the depth of the plastic deformation layer under the machined surface are closely related to the cutting force, and the strain hardening level and the depth of deformation are positively related to the resultant cutting force. Pawade et al. [29] found that the yield strength of the subsurface is greater than that of the base material, and its change trend is similar to that of the microhardness. Ezugwu and Tang [30] posted that the round insert would lead to a lower microhardness than the rhomboid insert, and they also reported that prolonged machining with a ceramic tool would give a higher microhardness to the machined

surface. Thakur et al. [31] studied the relationship between cutting parameters and work hardening in high-speed machining of Inconel 718 through experiments, and controlled work hardening by changing cutting parameters to increase tool life. Rinaldi et al. [32] built a physics-based model to analyze plastic deformation and microhardness during Inconel 718 machining.

Since the middle of the last century, residual stress has received increased attention. Some studies try to determine the machining-induced residual stress based on experiment efforts. M'Saoubi et al. [33] evaluated residual stress in metal machining and proposed that the main cause of residual stress is mechanical influence, and the second factor is thermal influence. Lavella and Berruti [34] studied the residual stress of Inconel 718 at different cutting speeds and feed rates and found that there is tensile residual stress near the machined surface between 10 and 50 μm , which become compressive residual stress as the depth increases. Madariaga et al. [35] observed that the tensile residual stress decreases as the tool wear increases, while the compressive residual stress layer increases. Coelho et al. [26] proposed the relationship between tool geometry and residual stress. It was found that when ceramic cutting tools with a 20° chamfer were used, the residual stress was compressed. Arunachalam et al. [36] found that the tensile residual stress in the surface processed by the mixed ceramic cutting tool is much greater than that of CBN cutting tools. When using CBN cutting tools, the depth of cut affects residual stress more easily than the cutting speed. Dry cutting will cause tensile residual stress, and coolant will reduce residual stress or bring compressive residual stress. Pusavec et al. [37] reported that lower temperatures would introduce greater compressive residual stress below the machined surface. Hua and Liu [38] studied the magnitude and direction of principal residual stress and tested tension-tension fatigue. It has been shown that the magnitude of the maximum principal residual stress is much larger than the magnitude of the surface residual stress along with the axial and circumferential directions, and its direction is close to the cutting axial direction and has a great influence on the fatigue life.

Some studies have also tried to give an analysis model to predict residual stress in 2D machining of Inconel 718. In 2000, Jacobus et al. [39] proposed an analytical model for residual stress. They gave a theory of how mechanical and thermal loads affect the generation of residual stress, and both mechanical and thermal loads are considered in the model. Ulutan et al. [40] published another method of predicting residual stress in orthogonal cutting. They utilized the plastic deformation model presented by Jiang and Sehitoglu [41] for elastoplastic materials under plane strain and the stress release procedure. Liang and Su [42] applied Oxley's slip field theory and considered the contribution of the ploughing force of the tool to the mechanical load. They assumed that the material is dynamically work-hardened and gave the distribution of residual stress with a hybrid algorithm which is presented by McDowell [43]. Based on the proposed analysis model, Wan et al. [44] presented residual stress in three-dimensional oblique milling. Huang, et al. [45] published an article about residual stress in orthogonal flank milling with a 0° helix angle. Ji et al. [46] offer a model for the residual stress prediction under minimum quantity lubrication (MQL) machining conditions.

On the other hand, it is becoming more and more common for residual stress prediction to use the finite element modeling (FEM) method and commercial software. Lin et al. [47] analyzed the stress field on the surface of the part during the machining process and utilized a thermal-mechanical coupling model in the finite element model. Lo [48] reported that an increase in the rake angle of the tool will result in an increase in the residual tensile stress in the cutting direction. Lin et al. [49] found that the increase in the flank wear length leads to an increase in the residual compressive stress on the machined surface. In the study presented by Sasahara et al. [50], the relationship between residual stress and the tool corner radius is analyzed with the FEM method. Artificial neural networks are incorporated into the model established by Umbrello et al. [51]. Li et al. [52] analyzed the relationship between cutting depth and residual stress in the milling of thin-walled parts in a software Advantage and found that the residual stress of the machined surface will decrease as the cutting

depth decreases. To shorten the simulation time of residual stress prediction, Yang et al. [53] introduced a statistical model in their hybrid FEM model.

1.4 Research problems and objectives

To cut Inconel 718 with high surface quality and efficient machining, it is very important to reduce residual stress and strain hardening in machining Inconel 718. However, the related research problem remains.

Work-hardening in machining Inconel 718 negatively affects surface integrity, such as yield strength, micro-hardness, tool wear, and machining efficiency. At present, the prediction methods of work hardening in Inconel 718 cutting are mainly based on experiments and empirical models. A research object is to establish a new model to obtain the work hardening behaviour of the material and predict the thickness and hardness of the work-hardened layer by analyzing the stress experience in the known cutting force and other cutting parameters.

The current analysis models of residual stress have some limitations. There is a gap between the current approaches and actual machining. The hardening of the workpiece material during machining can have an impact on its material properties and machinability. The effect of hardening of the surface layer in the prior machining is ignored when calculates residual stresses in the subsequent machining, which reduces the accuracy of the prediction of stresses and residual stresses. Therefore, a more accurate model is required to describe the residual stress in the machining process.

1.5 Thesis outline

In this thesis, Chapter 2 introduces a well-established stress modeling. In Chapter 3, the relationship between hardness and work hardening is discussed and a method to predict the hardness is introduced. Then present an improved method to residual stress. In Chapter 4 the prediction method is verified, and the application cases are studied.

CHAPTER 2 STRESS MODELING IN ORTHOGONAL CUTTING

2.1 Cutting force in orthogonal cutting

The cutting forces acting on the workpiece play an important part in metal cutting. The forces cause the workpiece material to deform and to be cut from the workpiece. Cutting forces are also the main resource of mechanical effects that result in residual stress and work hardening in the machined surface. A diagram of the orthogonal turning process is shown on the left side in Figure 2.1, and the detail after zoom-in is on the right side.

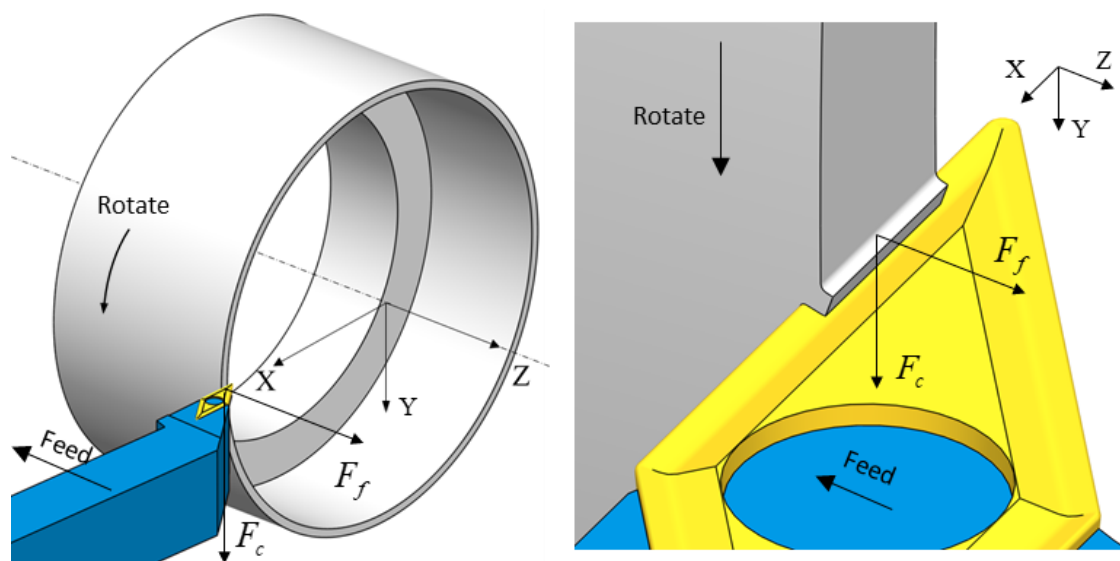


Figure 2.1 Cutting forces in orthogonal turning

Metal cutting is the machining operation that removes the material layer from the workpiece with the cutting tool. In the actual metal cutting, the external forces acting on the workpiece by the tool make some of the material of the workpiece

deform and separated from the workpiece by shearing to become the chip [54]. The boundary (AB in Figure 2.2) between the deformed and undeformed material is assumed to be straight and is called the shear plane. As shown in Figure 2.2, the chip above the shear plane is the deformed material that has undergone the shearing process, and the shear angle describes the angle ϕ between the shear plane and the direction of the cut.

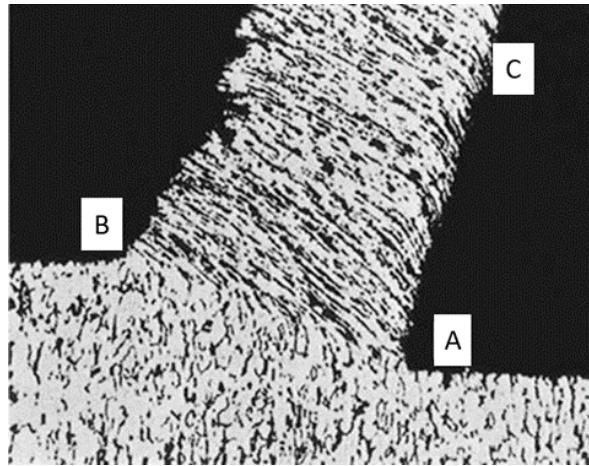


Figure 2.2 Micrograph of the partially formed chip of metal cutting

Orthogonal cutting has been ideally expressed in terms of a two-forces system. In Figure 2.1, F_t is the axial force which is parallel to the feed direction and F_c is the tangential force. The model of the ideal orthogonal cutting process is based on some assumptions includes:

- The cutting edge is a straight line and perpendicular to the direction of motion (Y-axis) which indicates the cutting speed.
- The shear and normal stresses are distributed on the shear plane and the tool-chip interface uniformly.
- The material does not spread to either side and the chip flow is parallel to the direction of cutting edge movement.

In summary, the ideal orthogonal cutting process could be treated as a plane strain problem, which means plastic deformation only exists in the YZ plane.

A cutting force modeling for the steady orthogonal cutting process is shown in Figure 2.3. The movement of chips from A to C is considered to be frictional sliding with a constant coefficient, and the force F_{cn} and F_{cs} are the normal force and the tangential force respectively there. If the chip is considered as an isolated free body, as the forces on the chip are balanced, the resultant force R of F_{cn} and F_{cs} should be equal to the force R' which is between the chip and the workpiece along the shear plane AB. Another part of the mechanical effect that causes residual stress is the wear of the rear tool face. In the actual metal cutting, the tool wears and makes frictional contact on the machined surface.

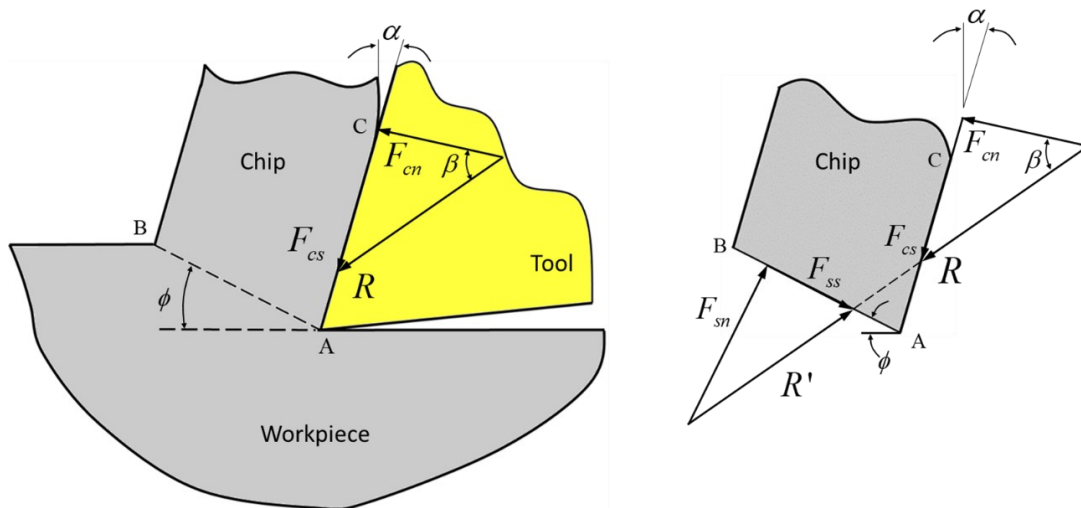


Figure 2.3 Cutting force modeling of orthogonal cutting

2.1.1 Cutting force prediction theory

Currently, a lot of research into the cutting force model has been published, and one of the widely used in residual stress prediction is based on the model presented by Su [55]. The cutting conditions are used as input for the model to predict

the cutting forces, and a modified algorithm is presented to determine the coefficients such as shear angle, etc. The theory is based on the chip formation model which is shown in detail in Figure 2.4.

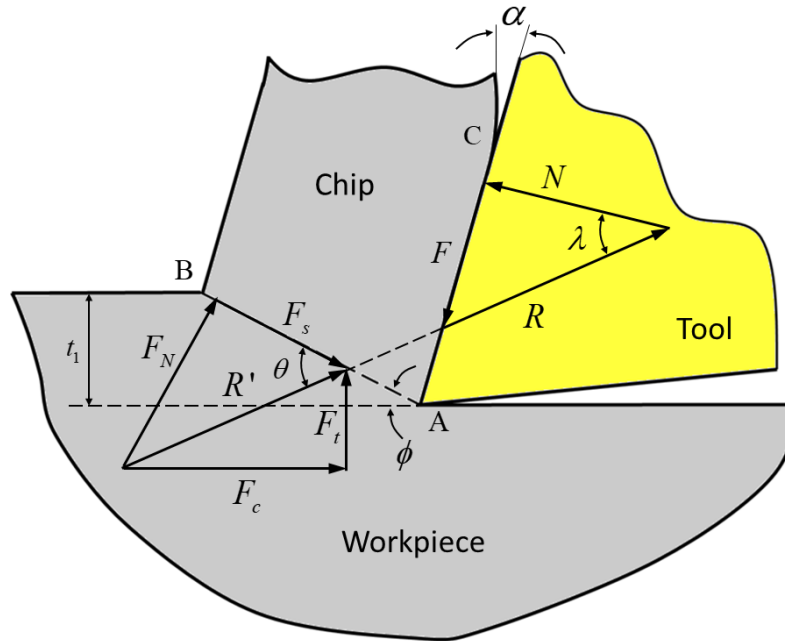


Figure 2.4 Chip formation model used in the analysis [42]

The cutting forces can be estimated by the following equations after the shear angle ϕ is defined, where α is the rake angle of the tool.

$$\begin{aligned}
 t_2 &= \frac{t_1 \cos(\phi - \alpha)}{\sin \phi} \\
 F_c &= R \cos(\lambda - \alpha) \\
 F_t &= R \sin(\lambda - \alpha) \\
 F &= R \sin \lambda \\
 N &= F \cos \lambda \\
 R &= \frac{F_s}{\cos \theta} = \frac{k_{AB} t_1 w}{\sin \phi \cos \theta}
 \end{aligned} \tag{2.1}$$

The velocity of the material flow of the chip and the shear plane is given by

$$\begin{aligned}
V_c &= \frac{V \sin \phi}{\cos(\phi - \alpha)} \\
V_s &= \frac{V \cos \alpha}{\cos(\phi - \alpha)}
\end{aligned}
\tag{2.2}$$

where V_c and V_s are the velocities of the material flow of the chip and the shear plane, respectively. Then the strain and the strain rate along the shear plane are given by

$$\begin{aligned}
\dot{\varepsilon}_{AB} &= \frac{V \cos \alpha}{\sqrt{3} \Delta s_1 \cos(\phi - \alpha)} \\
\varepsilon_{AB} &= \frac{\cos \alpha}{2\sqrt{3} \sin \phi \cos(\phi - \alpha)}
\end{aligned}
\tag{2.3}$$

As the machining process of Inconel 718 is accompanied by high stress, high strain and strain rate, and high temperature, the Johnson-Cook constitutive model is applied to approximate the flow stress in the cutting process. The model is a function of strain, strain rate and temperature. The general form of the J-C constitutive model is expressed as

$$\sigma = \frac{1}{\sqrt{3}} \left(A + B \varepsilon_p^n \right) \left(1 + C \ln \frac{\dot{\varepsilon}_p}{\dot{\varepsilon}_0} \right) \left(1 - \left(\frac{T - T_r}{T_m - T_r} \right)^m \right)
\tag{2.4}$$

where σ is the stress, ε_p is the plastic strain, $\dot{\varepsilon}_p$ is the plastic strain rate, $\dot{\varepsilon}_0$ is the reference plastic strain rate, T is the temperature of the material, T_r is the reference temperature (293 K), and T_m is the melting temperature of the workpiece material. The model also involves five material constants A , B , C , n , and m . Therefore, the flow stress along the shear plane is given by

$$k_{AB} = \frac{1}{\sqrt{3}} \left(A + B \varepsilon_{AB}^n \right) \left(1 + C \ln \frac{\dot{\varepsilon}_{AB}}{\dot{\varepsilon}_0} \right) \left(1 - \left(\frac{T_{AB} - T_r}{T_m - T_r} \right)^m \right)
\tag{2.5}$$

The average temperature along the shear plane AB can be determined from

$$T_{AB} = T_w + \eta \Delta T_{sz} \quad (2.6)$$

in which η is a factor about the ratio of the chip formation and η is 0.9, ΔT_{sz} is the temperature rise at the shear plane area and can be obtained by

$$\Delta T_{sz} = \frac{(1-\beta)F_s V_s}{\rho_{wk} V t_1 w C_p} \quad (2.7)$$

where C_p is the specific heat of the material, and β ($0 \leq \beta \leq 1$) is the proportion of heat conducted into the work which is given by

$$\beta = \begin{cases} 0.5 - 0.35 \log_{10}(R_T \tan \phi) & 0.004 \leq R_T \tan \phi \leq 10 \\ 0.3 - 0.15 \log_{10}(R_T \tan f) & R_T \tan f > 10 \end{cases} \quad (2.8)$$

in which R_T is a non-dimensional number determined by

$$R_T = \frac{\rho_{wk} C_p V t_1}{K_{wk}} \quad (2.9)$$

where K_{wk} is the thermal conductivity of the material.

The angle θ between the shear plane and the resultant force is defined by

$$\tan \theta = 1 + 2 \left(\frac{\pi}{4} - \phi \right) - C_{Oxley} n \frac{B \varepsilon_{AB}^n}{A + B \varepsilon_{AB}^n} \quad (2.10)$$

and the friction angle λ is expressed in terms of other angles by

$$\lambda = \alpha + \theta - \phi \quad (2.11)$$

During the cutting process, the shear stress along the shear plane AB is

considered to be equal to the flow stress of the material there, so the cutting forces can be obtained from Equation (2.5). And the normal stress at point B is given by

$$\sigma_N' = k_{AB} \left(1 + \frac{\pi}{2} - 2\alpha - 2C_{Oxley} n \frac{B\varepsilon_{AB}^n}{A + B\varepsilon_{AB}^n} \right) \quad (2.12)$$

For the tool-chip interface, the effective strain rate is given by

$$\dot{\varepsilon}_{int} = \frac{V_c}{\sqrt{3}\delta t_2} \quad (2.13)$$

and the tool-chip contact length is found from

$$h = \frac{t_1 \sin \theta}{\cos \lambda \sin \phi} \left(1 + \frac{C_{Oxley} n}{3 \tan \theta} \frac{B\varepsilon_{AB}^n}{A + B\varepsilon_{AB}^n} \right) \quad (2.14)$$

Thus, the average shear stress at the tool-chip interface is

$$\tau_{int} = \frac{F_c}{hw} \quad (2.15)$$

To solve for the cutting force equilibrium condition at the tool-chip interface, the normal stress at point B is also given by

$$\sigma_N = \frac{N}{hw} \quad (2.16)$$

The average temperature at the tool-chip interface is calculated by

$$T_{int} = T_w + \Delta T_{sz} + \Psi \Delta T_M \quad (2.17)$$

where Ψ ($0 < 1$) is a factor about the average temperature at the tool-chip interface and ΔT_M is the maximum temperature rise in the chip which can be obtained by

$$\log_{10} \left(\frac{\Delta T_M}{\Delta T_C} \right) = 0.06 - 0.195 \delta \sqrt{\frac{R_r t_2}{t_1}} + 0.5 \log_{10} \left(\frac{R_r t_2}{h} \right) \quad (2.18)$$

with ΔT_C the average temperature rises of the chip given by

$$\Delta T_C = \frac{F V_c}{\rho_{wk} V t_1 w C_p} \quad (2.19)$$

Therefore, the average flow stress of the material of the chip is found from

$$k_{chip} = \frac{1}{\sqrt{3}} \left(A + B \varepsilon_{int}^n \right) \left(1 + C \ln \frac{\dot{\varepsilon}_{int}}{\dot{\varepsilon}_0} \right) \left(1 - \left(\frac{T_{int} - T_r}{T_m - T_r} \right)^m \right) \quad (2.20)$$

where the effective strain rate of the chip is given by

$$\varepsilon_{int} = 2 \varepsilon_{AB} + \frac{1}{\sqrt{3}} \frac{h}{\delta t_2} \quad (2.21)$$

In this method, as the chip formation is in equilibrium, the shear angle ϕ should satisfy that the flow stress along the tool chip interface calculated from the J-C equation, is equal to the shear stress obtained from the resultant cutting force R . Then the factor C_{Oxley} is obtained when $\sigma_N = \sigma_N'$, and the shear angle ϕ could be determined from the condition that the cutting force F_c takes the minimum value. A flow chart for the prediction model is shown in Figure 2.5.

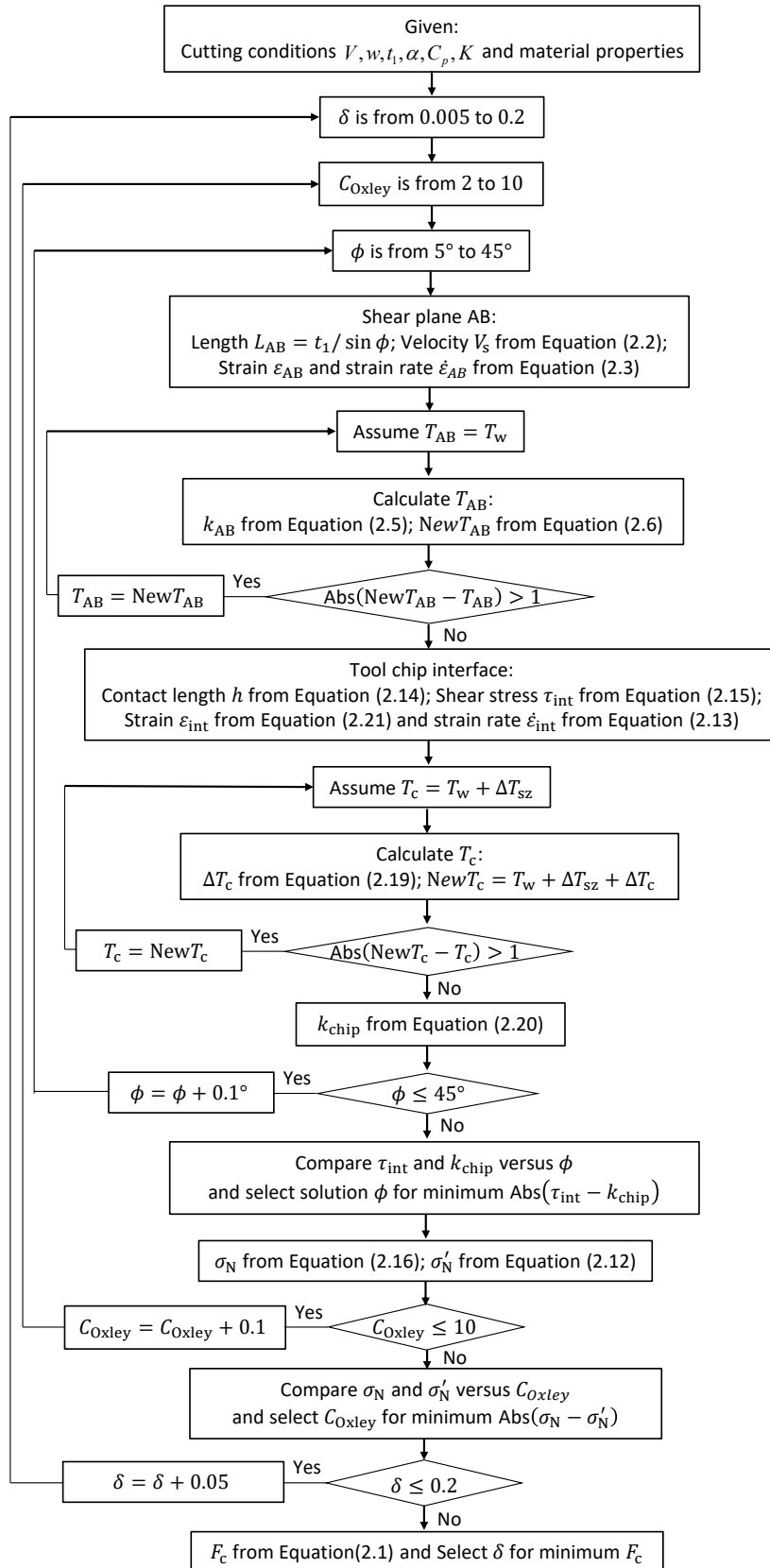


Figure 2.5 Flow chart of cutting force prediction model

2.1.2 Cutting force measurement

Although a lot of research about cutting force prediction has been published, these theories still have some limitations. To obtain the cutting force experimental means are also a common approach. Compared with the analytical prediction method, the cutting force test is more accurate and reliable. Some empirical models for predicting cutting forces are also based on cutting force measurement experiments. The cutting force is measured by the force-measuring equipment which can be installed in the cutting machine. At present, the widely used cutting force measurement devices are mainly resistance strain gauge dynamometer and piezoelectric dynamometer.

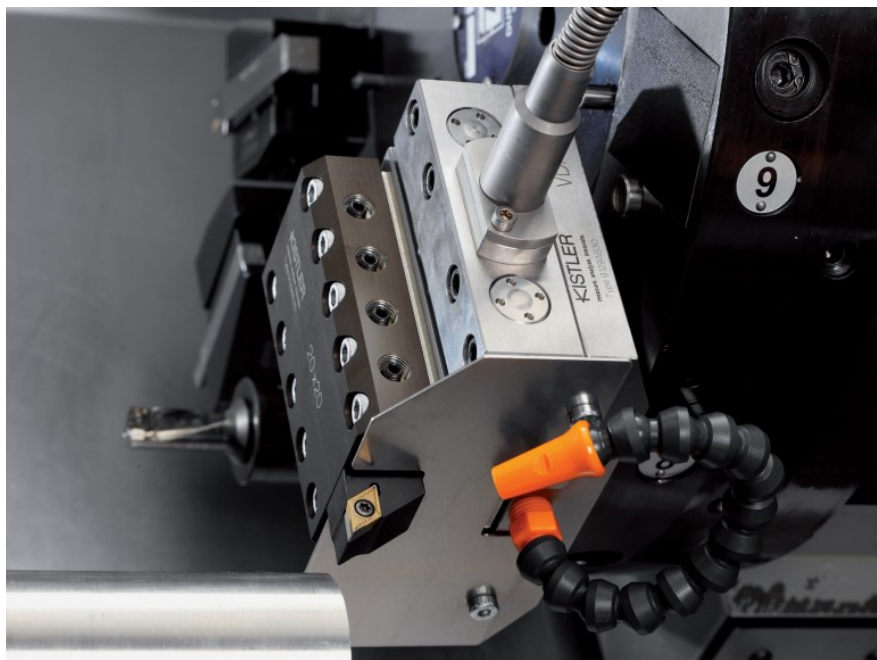


Figure 2.6 Cutting force dynamometer in a turning machine

The measurement technology of piezoelectric dynamometers (Figure 2.6) is based on the piezoelectric measurement principle [56]. The piezoelectric element in the sensor which is sensitive in the desired measurement direction is cut out of crystal or quartz material. The shear effect and longitudinal effect are both contribute to the

measurement. Crystals with cross-sections in the vertical direction are sensitive to the normal loads. When a normal force is applied to the longitudinal crystal disk, it will lead to a small shift in the center of gravity of the charge and generate a charge difference proportional to the load. Similarly, a charge difference will also arise in shear cross-sectional crystals if a shear load is employed. The charge amplifier will capture these measurable charge differences and output voltage signals.

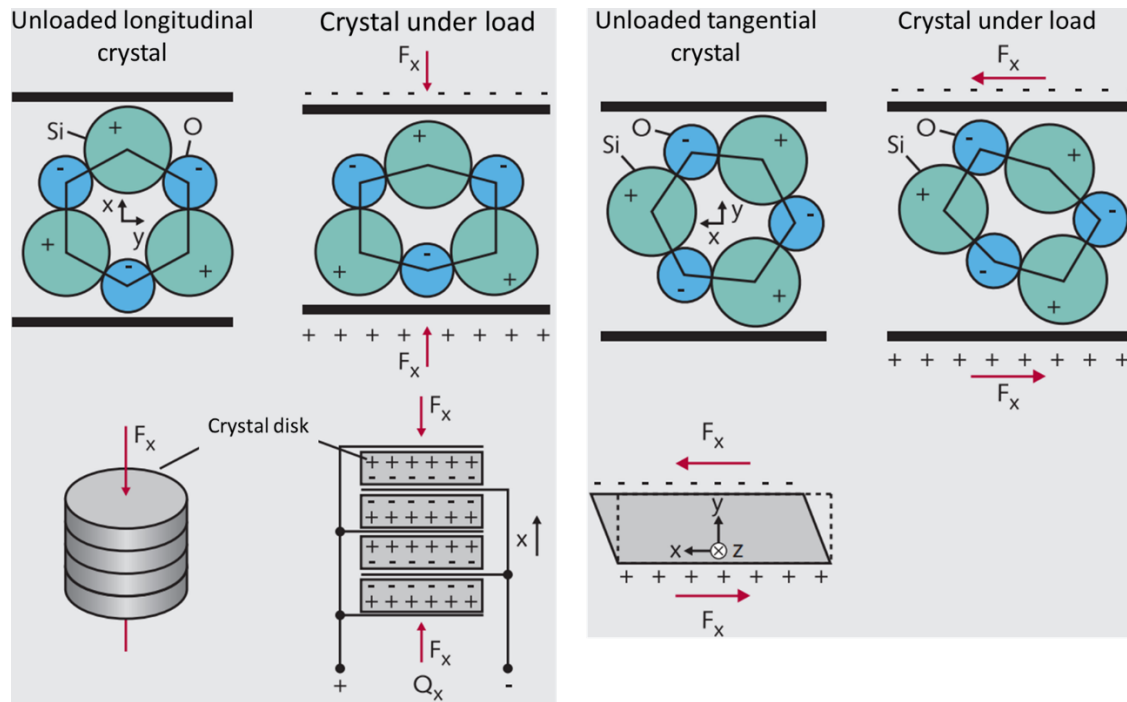


Figure 2.7 The measuring principle of the piezoelectric sensor

During the measuring process, the charge amplifiers will amplify the charge differences to a proportional voltage signal transmitted through connecting cables. Then the signal could be acquired and analyzed to show the cutting force in terms of graphics. The captured data can also be exported for further study. The whole measuring chain is presented in Figure 2.8.

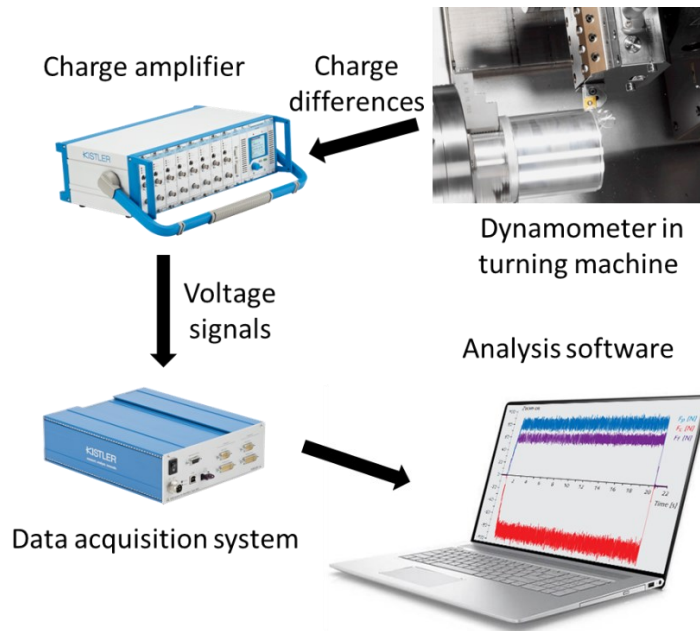


Figure 2.8 Measurement system for cutting force in turning

2.2 Stress modeling in orthogonal cutting

Although the cutting force may be relatively stable during the steady orthogonal cutting, the stress at a certain point in the workpiece material will change during the cutting process. For example, point M in Figure 2.9 (a) is getting close to the cutting edge and the profile of its changing stress may be like Figure 2.9 (b). Every point at the same depth in the material will have the same stress history. If the stress history at all depths can be obtained, then theoretically the stress history in the entire workpiece can be obtained. Therefore, the stress state can be found.

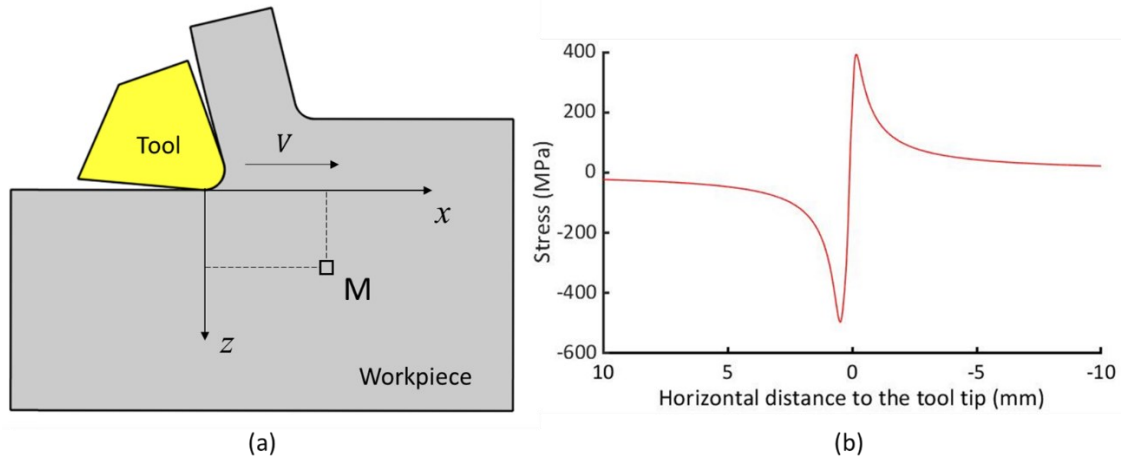


Figure 2.9 Contact stress history

The approach to the stress state is provided in the research of Su [55]. The basis of the approach to elastic stress is the contact theory. Under the plane strain condition, elastic stress components at any point throughout the solid are calculated by integrating the Boussinesq solution for both normal loads $p(s)$ and tangential loads $q(s)$ that act on the surface over the contact region from a to b (Figure 2.10). Then the elastic stresses are given by

$$\begin{aligned}
 \sigma_{xx} &= -\frac{2z}{\pi} \int_{-b}^a \frac{p(s)(x-s)^2}{[(x-s)^2 + z^2]^2} ds - \frac{2}{\pi} \int_{-b}^a \frac{q(s)(x-s)^3}{[(x-s)^2 + z^2]^2} ds \\
 \sigma_{zz} &= -\frac{2z^3}{\pi} \int_{-b}^a \frac{p(s)}{[(x-s)^2 + z^2]^2} ds - \frac{2z^2}{\pi} \int_{-b}^a \frac{q(s)(x-s)}{[(x-s)^2 + z^2]^2} ds \\
 \tau_{xz} &= -\frac{2z^2}{\pi} \int_{-b}^a \frac{p(s)(x-s)}{[(x-s)^2 + z^2]^2} ds - \frac{2z}{\pi} \int_{-b}^a \frac{q(s)(x-s)^2}{[(x-s)^2 + z^2]^2} ds
 \end{aligned} \tag{2.22}$$

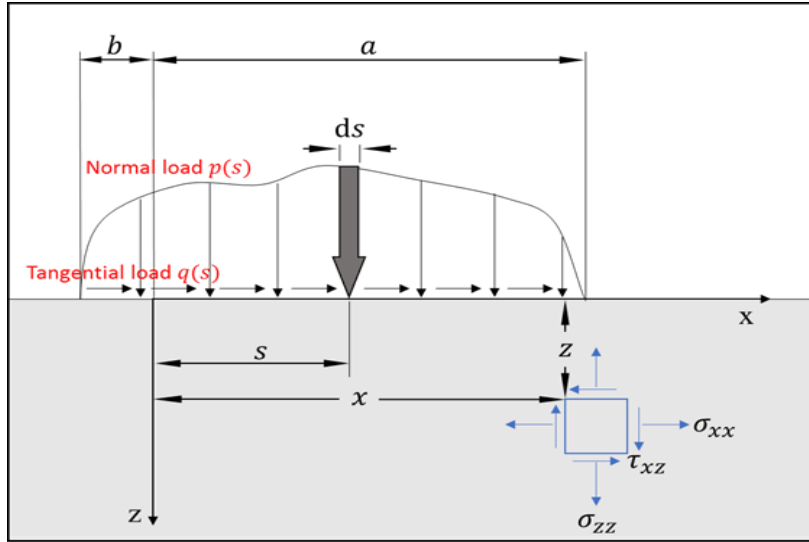


Figure 2.10 Contact model of boundary loads

As the orthogonal cutting process is assumed to be a plane strain, the tangential loads and the normal loads at the shear plane are given by

$$\begin{aligned}
 p_1 &= \frac{F_c \sin \phi + F_t \cos \phi}{L_{AB} w} \\
 q_1 &= \frac{F_c \cos \phi - F_t \sin \phi}{L_{AB} w}
 \end{aligned}
 \tag{2.23}$$

where F_c and F_t are chip formation forces obtained by Equation (2.1) or experimental means, ϕ is the shear angle, L_{AB} is the length of the shear plane, w is the cutting width. Then the stress resulted from the force acting on the shear plane (Figure 2.11) can be computed by

$$\begin{aligned}
 \sigma_{x_1 x_1} &= -\frac{2z_1}{\pi} \int_0^{L_{AB}} \frac{p_1(s)(x_1 - s)^2}{[(x_1 - s)^2 + z_1^2]^2} ds - \frac{2}{\pi} \int_0^{L_{AB}} \frac{q_1(s)(x_1 - s)^3}{[(x_1 - s)^2 + z_1^2]^2} ds \\
 \sigma_{z_1 z_1} &= -\frac{2z_1^3}{\pi} \int_0^{L_{AB}} \frac{p_1(s)}{[(x_1 - s)^2 + z_1^2]^2} ds - \frac{2z_1^2}{\pi} \int_0^{L_{AB}} \frac{q_1(s)(x_1 - s)}{[(x_1 - s)^2 + z_1^2]^2} ds \\
 \tau_{x_1 z_1} &= -\frac{2z_1^2}{\pi} \int_0^{L_{AB}} \frac{p_1(s)(x_1 - s)}{[(x_1 - s)^2 + z_1^2]^2} ds - \frac{2z_1}{\pi} \int_0^{L_{AB}} \frac{q_1(s)(x_1 - s)^2}{[(x_1 - s)^2 + z_1^2]^2} ds
 \end{aligned}
 \tag{2.24}$$

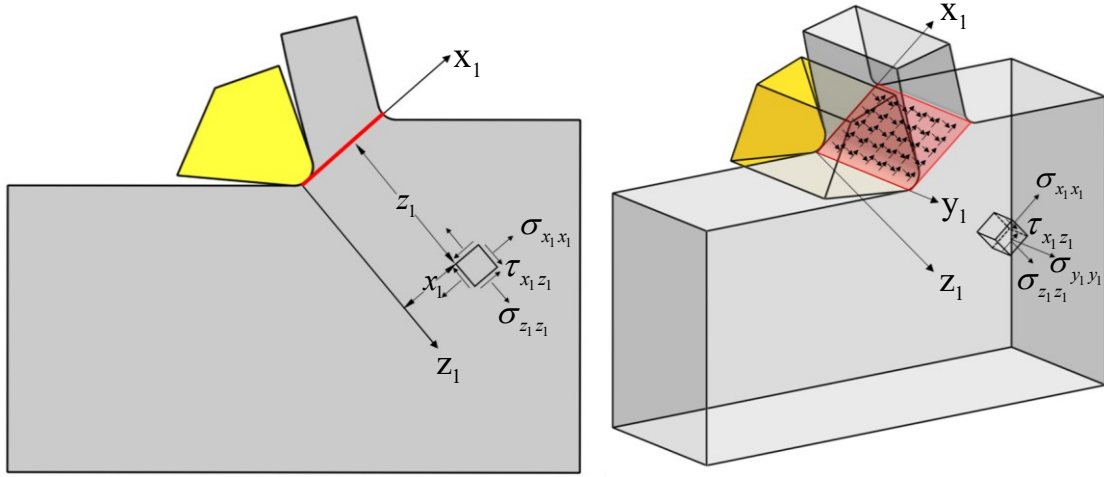


Figure 2.11 Stress components in the coordinate frame of the shear plane

Another part of mechanical stress is from the cutting edge contact area (Figure 2.12). The plowing force due to the chamfer of the cutting edge and the frictional force caused by the wear of the cutting tool are also contributed to the mechanical stress. The mechanical stress is calculated by Equation (2.25) below where $p_2(s)$ and $q_2(s)$ are the loads depends on the specific force distribution over the contact region.

$$\begin{aligned}
 \sigma_{x_2x_2} &= -\frac{2z_2}{\pi} \int_0^{L_{AB}} \frac{p_2(s)(x_2 - s)^2}{[(x_2 - s)^2 + z_2^2]^2} ds - \frac{2}{\pi} \int_0^{L_{AB}} \frac{q_2(s)(x_2 - s)^3}{[(x_2 - s)^2 + z_2^2]^2} ds \\
 \sigma_{z_2z_2} &= -\frac{2z_2^3}{\pi} \int_0^{L_{AB}} \frac{p_2(s)}{[(x_2 - s)^2 + z_2^2]^2} ds - \frac{2z_2^2}{\pi} \int_0^{L_{AB}} \frac{q_2(s)(x_2 - s)}{[(x_2 - s)^2 + z_2^2]^2} ds \quad (2.25) \\
 \tau_{x_2z_2} &= -\frac{2z_2^2}{\pi} \int_0^{L_{AB}} \frac{p_2(s)(x_2 - s)}{[(x_2 - s)^2 + z_2^2]^2} ds - \frac{2z_2}{\pi} \int_0^{L_{AB}} \frac{q_2(s)(x_2 - s)^2}{[(x_2 - s)^2 + z_2^2]^2} ds
 \end{aligned}$$

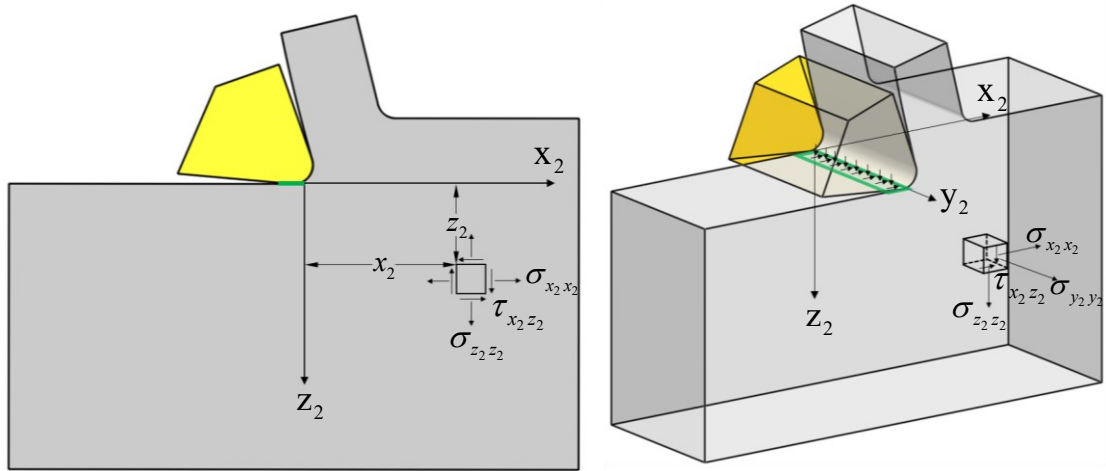


Figure 2.12 Stress components in the coordinate frame of the cutting edge contact area

A coordinate transformation is required to combine the stresses respectively calculated from the different coordinate frames above ($\{x_1y_1z_1\}$ and $\{x_2y_2z_2\}$) into the coordinate frame $\{xyz\}$. Figure 2.13 shows the relationship between the two coordinate frames.

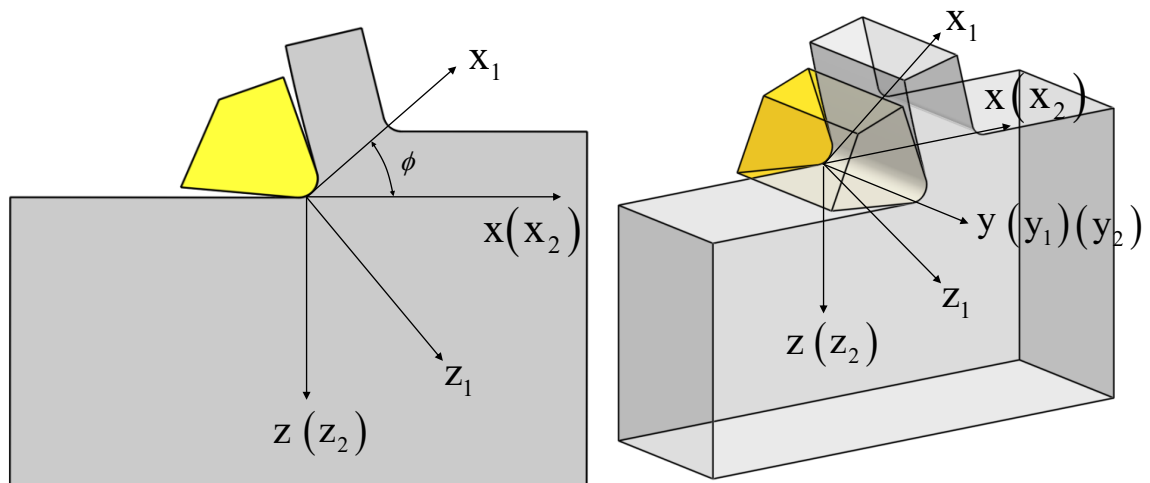


Figure 2.13 Geometric relationship of the coordinate frames

Equation (2.26) denotes the stress predicted from the shear plane zone and the cutting edge contact area. The transformation matrix presented in Equation (2.27)

is used to transform the stress in the coordinate frames $\{x_1, y_1, z_1\}$ to the coordinate frame $\{xyz\}$. Then the combination of the stress in the coordinate frame $\{xyz\}$ is given by Equation (2.28).

$$[\sigma_1] = \begin{bmatrix} \sigma_{x_1 x_1} & \tau_{x_1 z_1} \\ \tau_{x_1 z_1} & \sigma_{z_1 z_1} \end{bmatrix}, [\sigma_2] = \begin{bmatrix} \sigma_{x_2 x_2} & \tau_{x_2 z_2} \\ \tau_{x_2 z_2} & \sigma_{z_2 z_2} \end{bmatrix} \quad (2.26)$$

$$Q = \begin{bmatrix} \cos \phi & \sin \phi \\ -\sin \phi & \cos \phi \end{bmatrix} \quad (2.27)$$

$$\begin{bmatrix} \sigma_{xx} & \tau_{xz} \\ \tau_{xz} & \sigma_{zz} \end{bmatrix} = [\sigma] = Q[\sigma_1]Q^T + [\sigma_2] \quad (2.28)$$

As mentioned before, the strain in y direction i.e., ε_{yy} is 0 to satisfy the plane strain condition. Therefore, Hooke's law is employed here to find the corresponding stress component

$$\sigma_{yy} = \nu(\sigma_{xx} + \sigma_{zz}) \quad (2.29)$$

When the interested point getting closer to the cutting edge, the stress value of the point increases and exceeds the elastic limit. Here von Mises yield criterion is applied to decide if the material yields

$$f(\sigma_{ij}) = J_2 - k_0^2 \quad (2.30)$$

where k_0 is the initial shear yield stress and J_2 is the second invariant of the stress deviator tensor

$$J_2 = \frac{1}{2} S_{ij} S_{ij} \quad (2.31)$$

When the material yields, elastic-plastic loading occurs and the incremental plastic theory is utilized to obtain the plastic strain increment as shown in Equation (2.32). h is the plastic modulus, k is the subsequent yield stress in pure shear. S_{ij} is the component of deviatoric stress which is given in Equation (2.33). The isotropic hardening rule is employed here to describe the work hardening behaviour of the material. More details about work hardening and hardening rules are introduced in Chapter 3.

$$d\varepsilon_{ij}^p = \frac{1}{2hk^2} S_{ij} S_{kl} dS_{kl} \quad (2.32)$$

$$S_{ij} = \sigma_{ij} - \frac{1}{3} \delta_{ij} S_{kk} \quad (2.33)$$

As the plane strain condition is imposed, the strain component increment transverse to the direction of the cutting speed of the elastic-plastic state is given by

$$\begin{aligned} d\varepsilon_{yy} &= d\varepsilon_{yy}^e + d\varepsilon_{yy}^p \\ &= \frac{1}{E} [d\sigma_{yy} - \nu(d\sigma_{xx} + d\sigma_{zz})] \\ &+ \frac{S_{yy}}{2hk^2} (S_{xx} d\sigma_{xx} + S_{yy} d\sigma_{yy} + S_{zz} d\sigma_{zz} + 2S_{xz} d\tau_{xz}) = 0 \end{aligned} \quad (2.34)$$

where $d\varepsilon_{yy}^e$ and $d\varepsilon_{yy}^p$ represent the elastic strain increment and plastic strain increment, respectively. Consequently, the stress increment is expressed in

$$d\sigma_{yy} = \frac{\left[\left(\nu - \frac{E}{2hk^2} S_{xx} \right) d\sigma_{xx} + \left(\nu - \frac{E}{2hk^2} S_{zz} \right) d\sigma_{zz} - \frac{E}{2hk^2} S_{xz} d\tau_{xz} \right] S_{yy}}{1 + \frac{ES_{yy}^2}{2hk^2}} \quad (2.35)$$

in which the stress increments in the other directions are assumed to be equal to the

elastic stress components, which means

$$d\sigma_{xx} = d\sigma_{xx}^e, d\sigma_{zz} = d\sigma_{zz}^e, d\tau_{xz} = d\tau_{xz}^e \quad (2.36)$$

where $d\sigma_{ij}^e$ is calculated from the elastic contact model.

In the stress algorithm for the material in the region of interest, a strategy like “layer-by-layer scanning” is used. For a layer of material at a certain depth z (Figure 2.14), the arbitrary point in that layer moves from a far location toward the tool. This movement is assumed to be uniformly divided into many steps and the length of each step is Δx . The calculation starts when x takes the initial value. For each cycle of the calculation, the value x is increased by one step and substituted into the equations to calculate the stress. The value x is continuously increased and the corresponding stress value is updated until $x = x_{\text{final}}$, then the stress state history of the point is found.

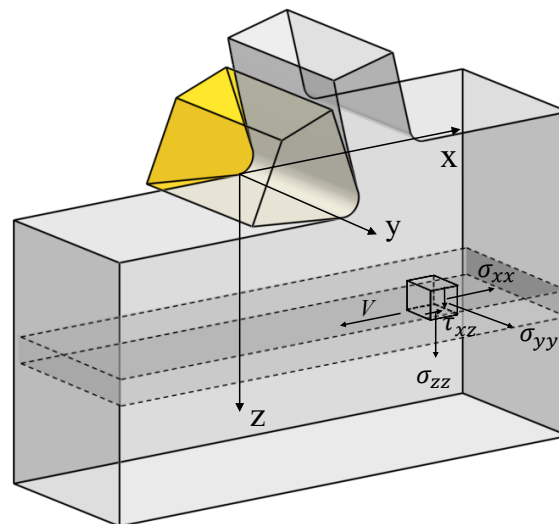


Figure 2.14 Stress state for the arbitrary point in the material layer at a certain depth

Since the material layer at the same depth will sequentially and successively experience the same stress state, the stress state history of the point obtained in the

above calculation can also be used to describe the stress state of the layer at that depth at a certain moment. Then the above process is repeated to calculate the stress state history for the next layer until the stress state history is found for all depths. Then the stress state history of the material in the entire region of interest during the cutting process can be obtained. The flow chart of the algorithm is presented in Figure 2.15.

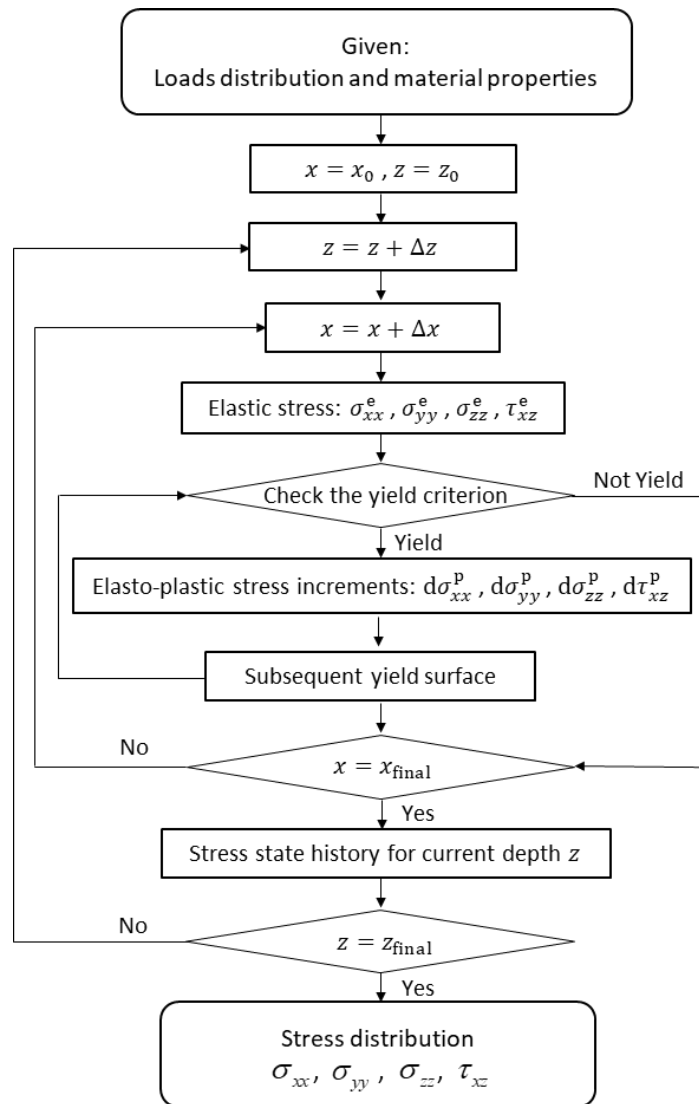


Figure 2.15 Simplified flow chart for the algorithm of the stress

CHAPTER 3 HARDNESS AND RESIDUAL STRESS

MODELING

3.1 Material yield and work-hardening

3.1.1 Material yield criterion

In uniaxial tensile testing, the determination of whether a material has yielded is made by direct comparison of stress and yield strength. However, sometimes the stress state of the material can be more complex, for example in Figure 3.1, the direction of the stress vector OQ does not coincide with any of the coordinate axes in the six-dimensional space of stresses. Nevertheless, the elastic boundary of the material will still form a region in this coordinate system. When the stress is inside this region, the material is in an elastic state. When the stress reaches the boundary of this region, the material yields and plastic deformation occurs, and this boundary is the yield surface.

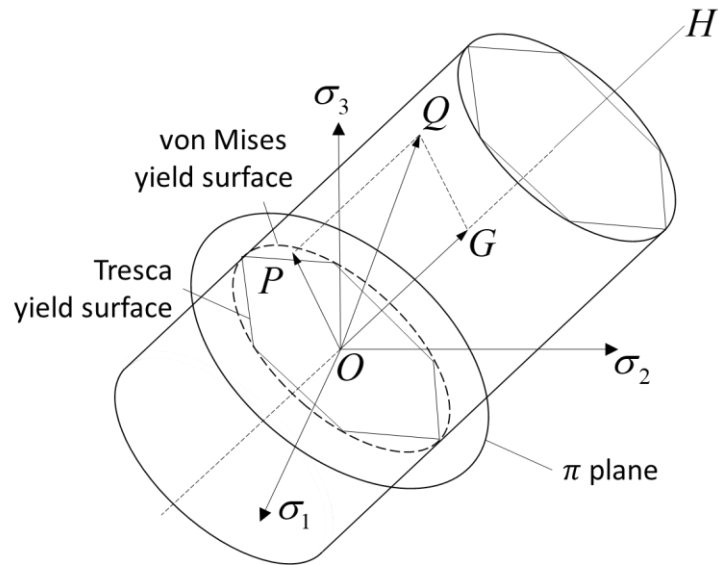


Figure 3.1 Yield surface in the stress space

The yield surfaces correspond to the yield criteria. The commonly utilized yield criteria are von Mises yield criteria and Tresca yield criteria. von Mises yield criterion is expressed as Equation (3.1). He suggested that the cross-section of the yield surface was a circle and any point on the axis of the yield surface satisfies $\sigma_1 = \sigma_2 = \sigma_3$. So, whether the loaded material yields or not depends on the magnitude of the projection on the π plane of the stress vector.

$$f = \frac{1}{2} S_{ij} S_{ij} - k^2 \quad (3.1)$$

3.1.2 Work-hardening

In some metalworking processes, such as rolling, the yield strength and hardness of the plastic deformed material increase because of work hardening [57]. The stress-strain curve of the material loaded to yield and then unloaded is shown on the left side of Figure 3.2. After unloading, the elastic deformation is released while the plastic deformation remains in the material. When the material is loaded again,

the modulus of elasticity is the same value but the stress at the yield point is higher. The strengthening that takes place in the plastically deformed material is called work hardening.

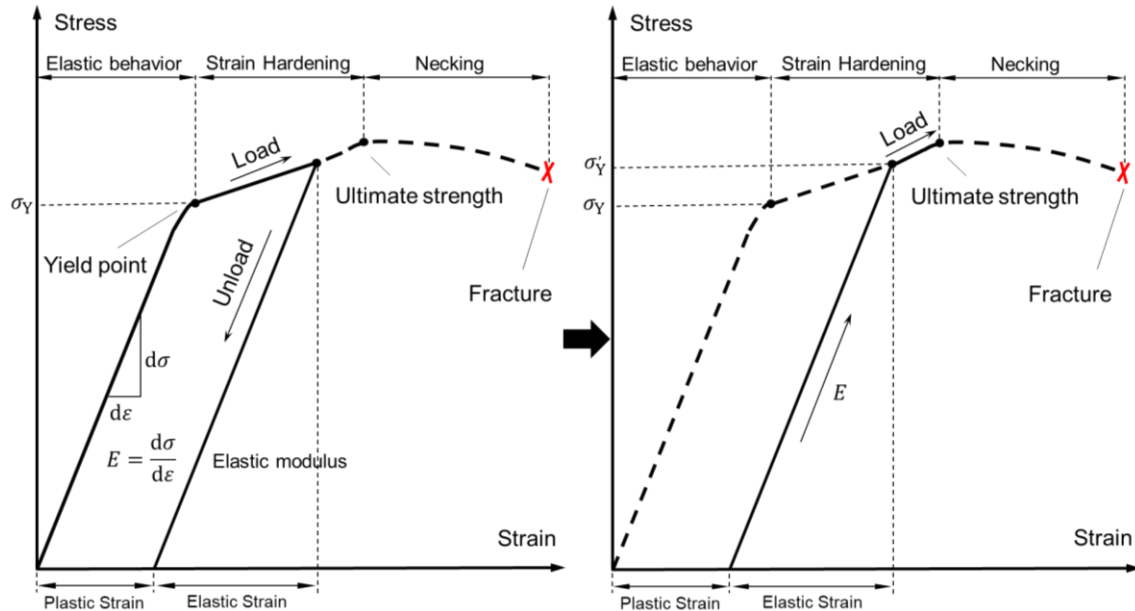


Figure 3.2 Stress-strain curve of the work-hardened material

Plastic deformation of metals is often executed by the motion of dislocations. Dislocations are linear defects within the crystal which include edge dislocation, screw dislocation and mixed dislocation. Figure 3.3 shows the motion of different types of dislocations.

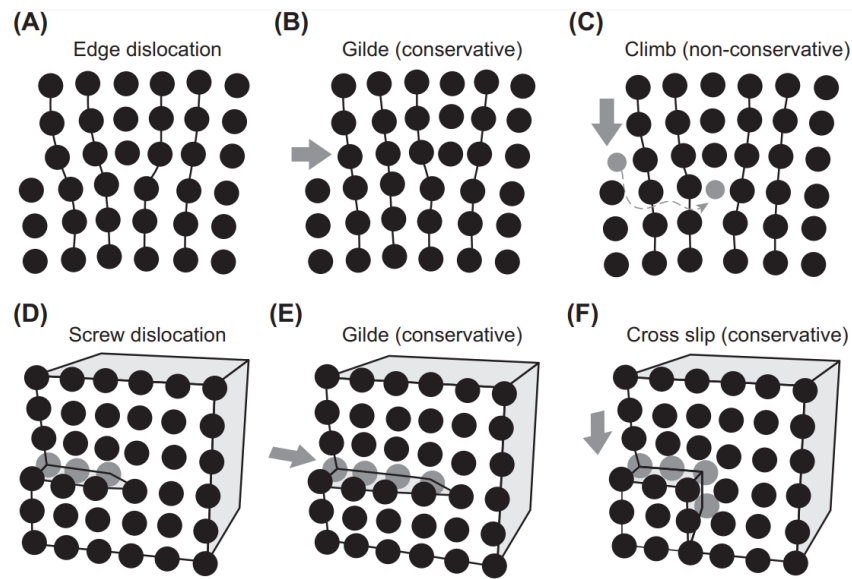


Figure 3.3 Dislocations and their motions [58]

During plastic deformation, the density of dislocations increases with the slip of dislocations. The dislocations are entangled with each other which will decrease the mobility of dislocations. On the other hand, the grain boundary and the impurity atom will hinder the slip of dislocations [59]. These interactions mentioned above lead to increased resistance of the material to dislocation motion. Therefore, greater stress is required to continue the motion of the dislocation to carry out further plastic deformation, which means the material is strengthened during the plastic deformation.

3.2 Hardness modeling

3.2.1 Hardness measurement

Hardness refers to the ability of a material to partially resist a hard object being pressed into its surface [62]. The hardness of the material can be compared by the hardness test. The resistance of the deformation is given by

$$H = \frac{F}{A} \quad (3.2)$$

in which F is the external load applied on the hard object and A is the indentation on the material surface. Figure 3.4 shows the impression induced by the indenter in the hardness test [57].

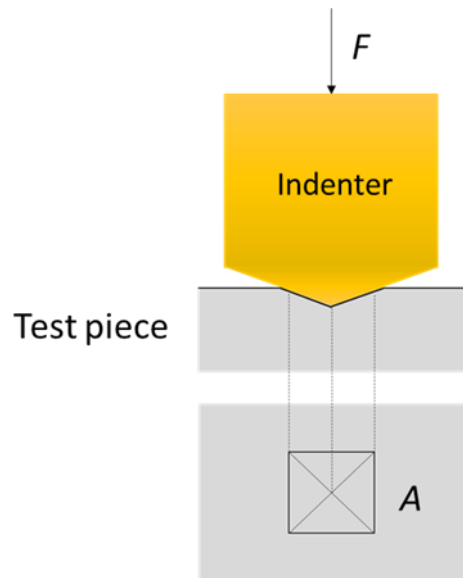


Figure 3.4 Steel indenter forced on the surface in the hardness test

3.2.2 Hardness modeling in orthogonal cutting

The plastic deformation during the machining process leads to work hardening and has effects on the yield strength and hardness. On the other hand, the definition of hardness illustrates that the hardness of the material is affected by its resistance to plastic deformation, and the yield strength describes the limit of the stress for the plastic deformation to take place. In the hardness test, a hard project (indenter) is impressed into the material and the material plastically deforms and an indentation is produced. The value of hardness equals the ratio of the load to the indentation size. During the machining process, plastic deformation occurs after the material yields,

and the material is work hardened. The yield strength of work-hardened material increases, and that leads to a rise in the resistance to plastic deformation. As shown in Figure 3.5, when the material is work-hardened, If we measure the hardness of the work-hardened material, we could find that the size of the indentation would be smaller than that of unhardened material. because it is more difficult to produce plastic deformation on the work-hardened material. Therefore, hardness will increase when the material is work-hardened. In metal machining, the change of hardness illustrates the degree of work hardening. We can evaluate the work hardening of the machined surface by calculating the hardness.

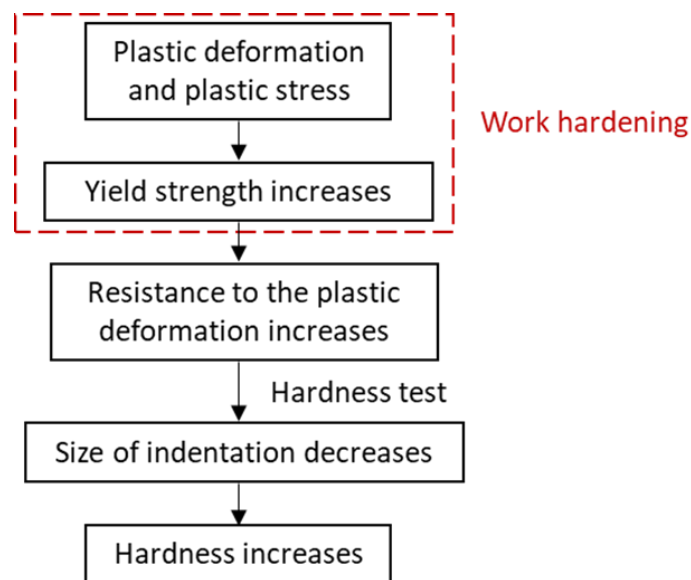


Figure 3.5 Work hardening and hardness

A model to predict the hardness of the machined surface of Inconel 718 is given below. Based on the relationship between hardness and yield strength, this model uses yield strength to obtain hardness. An equation is provided to describe the relationship between the microhardness and the ultimate strength in Equation (3.3) [29].

$$\sigma_u \equiv H/2.9 \left[1 - (m-2) \right] \left[\frac{12.5(m-2)}{1 - (m-2)} \right]^{(m-2)} \quad (3.3)$$

where m is the Meyer index.

On the other hand, a relation between the ultimate strength and the yield strength is utilized and C is a constant [29]

$$\sigma_y = C\sigma_u \quad (3.4)$$

therefore, the yield strength is expressed as

$$\sigma_y = C \left\{ H/2.9 [1 - (m-2)] \left[\frac{12.5(m-2)}{1 - (m-2)} \right]^{(m-2)} \right\} \quad (3.5)$$

If the Meyer index is substituted in terms of hardening coefficient n , as $m-2 = n$, the yield strength is given by

$$\sigma_y = C \left\{ H/2.9 [1 - n] \left[\frac{12.5n}{1 - n} \right]^n \right\} \quad (3.6)$$

Therefore, hardness can be expressed in terms of yield strength. Once the stress and work hardening histories of the material during cutting are captured, the thickness of the layer of the work-hardened material and the hardness value under the machined surface can be found.

3.3 Residual stress in machining

Some metalworking processes lead to plastic deformation takes place in the material of the part. After the metalworking process, the part is free from the load worked on it. However, the plastic deformation is left in the part. This plastic deformation induces the part to have residual stress. If categorized according to scale,

this type of residual stress belongs to type I or macroscopic residual stress (Figure 3.6). The operations that remove material from the workpiece, for example, metal cutting and grinding, could result in residual stress. Besides, plastic deformation and residual stress also exist in metal fabrications without chip formation such as extrusion and welding. The plastic deformation and residual stress generated in the machining process have effects on the cracks, fractures and fatigue life of the part, and may even result in the significant deviation of the geometric features.

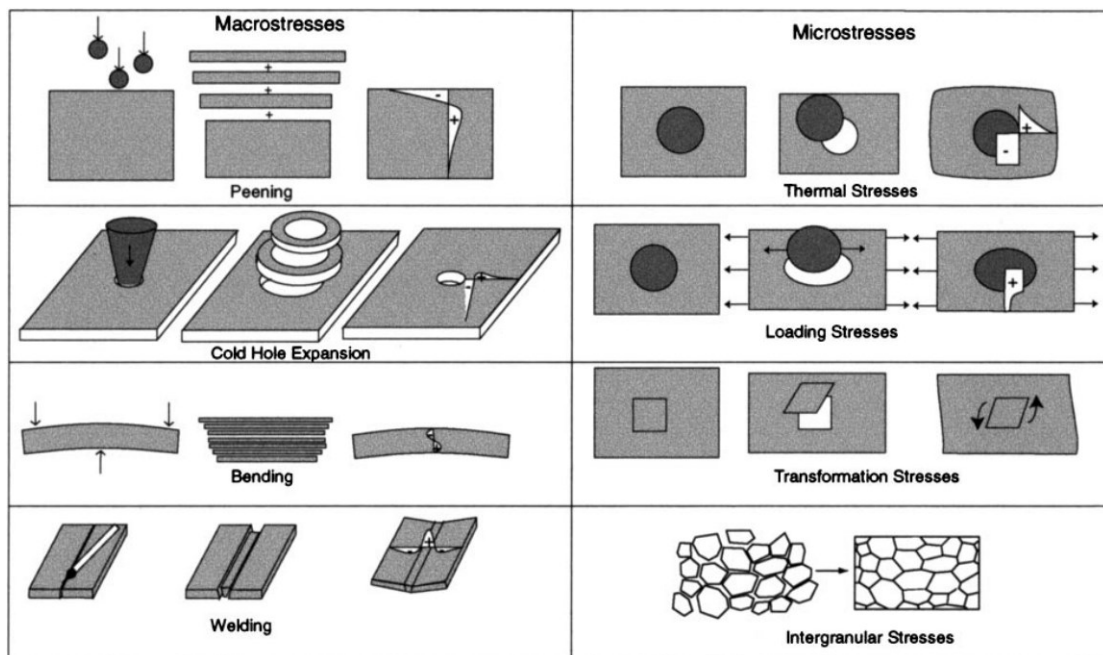


Figure 3.6 Residual macro stress (type I) and residual micro stress in grain scale (type II or intergranular stresses) [63]

The machining-induced residual stress is considered to be caused by un-uniform deformation. As shown in Figure 3.7 [39], the different layers beneath the machined surface are affected by different effects and result in different deformation during the machining process. After the machining process is finished, elastic deformation is released but plastic deformation remains in the body. When each layer is isolated individually, they would show varying degrees of deformation. However, these layers are not independent of each other but belong to the same body. For the

continuity and consistency of the material, there are interactions between these layers, which are manifested in the form of residual stress.

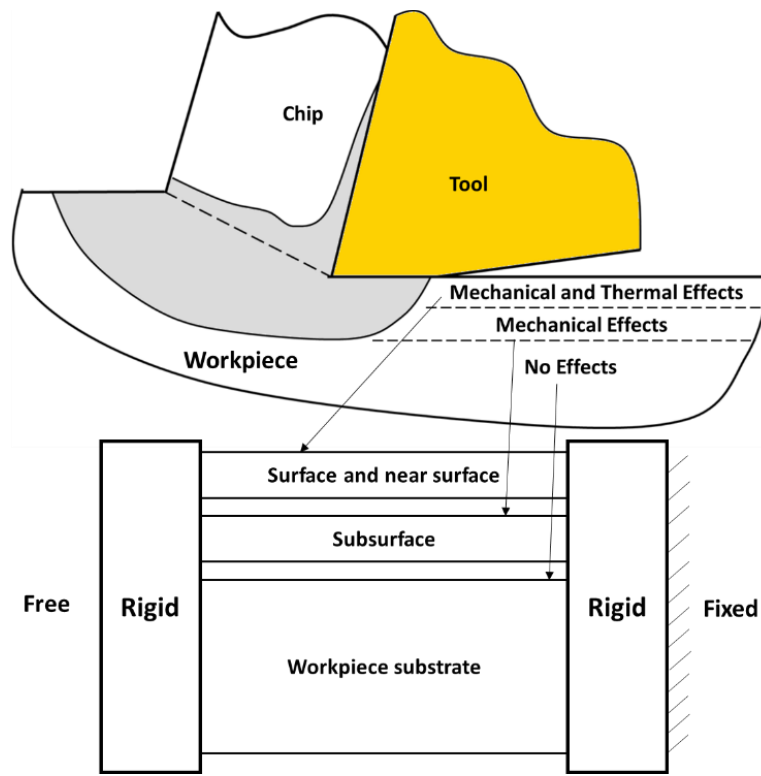


Figure 3.7 Schematic diagram of the generation of residual stress in machining proposed by Jacobus

However, the publications illustrated that the development of residual stress is more complicated than the theoretical suppose above [64]. A lot of research has been published on the measurement and prediction of residual stresses in metal machining. There are various results of the distribution of residual stress including direction (compression and tension), peak value and depth. The variation is related to the parameters and conditions of the machining process. Generally, the residual stress in the surface and the near face layer is tensile and then gradually becomes compression in the deeper layer. As the depth increases from about 50 mm to 200 mm, residual stress also decreases from its greatest compression towards 0.

3.4 Residual stress modeling in orthogonal cutting

In actual machining, workpiece surfaces are usually created by multi passes. The material will be work-hardened due to the cutting force during the machining pass and its initial properties such as will change. After one machining pass, the effect of work hardening on the workpiece material will remain in the workpiece. Therefore, in the subsequent pass, the cutting tool is cutting the material that has been hardened in the prior pass (Figure 3.8). Considering the effect of work hardening on the material properties described above, the analytical method for predicting residual stress is improved when calculating the residual stress induced by subsequent processing.

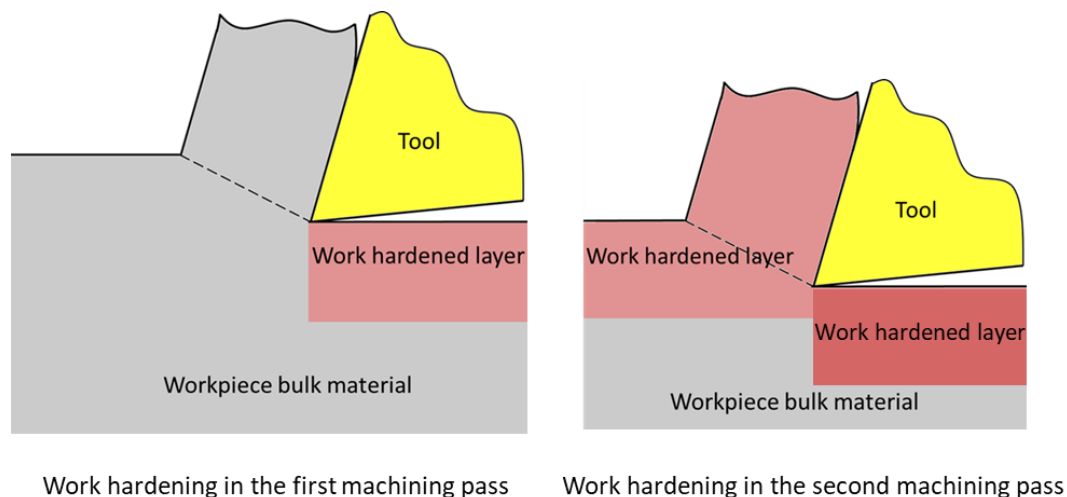


Figure 3.8 Work hardening in the first machining and second machining

After the tool passed the point of interest, the stress components σ_{ij} are not the residual stress what is desired. To satisfy the equilibrium conditions, a relaxation procedure is necessary for the stress and strain after loading [43].

First, the orthogonal cutting process is considered as a plane strain problem, so the strain in the y direction does not exist and the other components are independent of y where r denotes the residual components

$$\varepsilon_{yy}^r = 0 \quad (3.7)$$

Second, there is no traction on the machined surface so that the stress components including the shear stress and normal stress on the surface must be zero.

$$\tau_{xz}^r = \sigma_{zz}^r = 0 \quad (3.8)$$

As the machined surface retains a continuous plane, the strain component in the x direction also equals zero, and the other components are independent of x

$$\varepsilon_{xx}^r = 0 \quad (3.9)$$

Therefore, the rest of the components are residual stress and strain and can be expressed as

$$\begin{aligned} \sigma_{xx}^r &= f_1(z) & \sigma_{yy}^r &= f_2(z) \\ \varepsilon_{zz}^r &= f_3(z) & \varepsilon_{xz}^r &= f_4(z) \end{aligned} \quad (3.10)$$

where the $f(z)$ is the function of the depth z beneath the machined surface. However, the components calculated from the stress modeling is not satisfied the boundary conditions provided above. Therefore, these components would be relaxed incrementally and the values after the relaxation procedure are the residual stresses that remain under the machined surface.

If the relaxation consists of M steps, the relaxation procedure of the zero residual components is given by

$$\begin{aligned} \varepsilon_{xx}^r &= 0 \\ \tau_{xz}^r &= 0 \\ \sigma_{zz}^r &= 0 \end{aligned} \quad (3.11)$$

thus, the increments of each step are

$$\begin{aligned}\Delta \varepsilon_{xx} &= -\frac{\varepsilon_{xx}}{M} \\ \Delta \tau_{xz} &= -\frac{\tau_{xz}}{M} \\ \Delta \sigma_{zz} &= -\frac{\sigma_{zz}}{M}\end{aligned}\tag{3.12}$$

If the relaxation is elastic the increments can be written with Hook's Law as

$$\begin{aligned}\Delta \sigma_{xx} &= \frac{E\Delta \varepsilon_{xx} + \nu(1+\nu)\Delta \sigma_{zz}}{1-\nu^2} \\ \Delta \sigma_{yy} &= \nu(\Delta \sigma_{xx} + \Delta \sigma_{zz})\end{aligned}\tag{3.13}$$

otherwise, the increments are given by solving the equations below simultaneously

$$\left\{ \begin{aligned} &\left(\frac{S_{xx}S_{xx}}{2hk^2} + \frac{1}{E} \right) \Delta \sigma_{xx} + \left(\frac{S_{xx}S_{yy}}{2hk^2} - \frac{\nu}{E} \right) \Delta \sigma_{yy} = \\ &\Delta \varepsilon_{xx} - \left(\frac{S_{xx}S_{zz}}{2hk^2} - \frac{\nu}{E} \right) \Delta \sigma_{zz} - \frac{S_{xx}S_{xz}}{hk^2} \Delta \tau_{xz} \\ &\left(\frac{S_{yy}S_{xx}}{2hk^2} - \frac{\nu}{E} \right) \Delta \sigma_{xx} + \left(\frac{S_{yy}S_{yy}}{2hk^2} + \frac{1}{E} \right) \Delta \sigma_{yy} = \\ &-\left(\frac{S_{yy}S_{zz}}{2hk^2} - \frac{\nu}{E} \right) \Delta \sigma_{zz} - \frac{S_{yy}S_{xz}}{hk^2} \Delta \tau_{xz} \end{aligned} \right.\tag{3.14}$$

CHAPTER 4 VERIFICATION AND APPLICATION

4.1 Verification with the orthogonal cutting of AISI 316L

4.1.1 Introduction to a conventional experiment of cutting AISI 316L

AISI 316L is stainless steel widely used in industry. Its physics and mechanical properties are listed in Table 4.1. Similar to Inconel 718, AISI 316L is also sensitive to work hardening and residual stress. Inconel 718 is extremely expensive and inaccessible to civilians, and AISI 316L is quite popular and cheap in industry. Therefore, many researchers have employed AISI 316L, instead of using Inconel 718, to predict residual stress on the machined surface. For example, the FEA method, the experiment method, and the analytical method are applied to AISI 316L. In particular, the same cutting parameters of a paper published by Huang et al. are adopted [25]. This research work is introduced in the following. Table 4.2 gives the machining conditions of cutting AISI 316L. The cutting speed is 60 m/min, the tool feed rate is 0.1 mm/rev, and the cutting width is 3 mm.

Table 4.1 Properties of AISI 316 L

Young's modulus (GPa)	177
Poisson's ratio	0.3
Initial Von-Mises stress (MPa)	514
Plastic Modulus (GPa)	77
Density (kg/m³)	7750
Specific Heat Capacity (J/kg·°C)	500
Thermal Conductivity (W/m·K)	16.2

Table 4.2 AISI 316L cutting conditions

Cutting speed (m/min)	60
Feed (mm/rev)	0.1
Cutting width (mm)	3
Tangential force (N)	1117
Feed force (N)	726
Tangential cutting force (N)	1056
Normal cutting force (N)	422
Tangential edge force (N)	60
Normal edge force (N)	303
Chip thickness (mm)	0.35
Shear angle ϕ (degree)	15.9
Contact length on the flank face VB (mm)	0.06

Based on the parameters, first Huang calculated the stresses (σ_{xx} , σ_{yy} , σ_{zz} and σ_{xz}) in the region between the point in front of the cutting point along the tangential direction by 1.2 mm to the point at the back of the cutting point by -0.6 mm. Their stress curves are plotted in Figure 4.1. Then, the von Mises stress in the surface layer with a thickness of 0.18 mm in the region is calculated, and the stress distribution diagram is plotted in Figure 4.2. The von Mises stress at the point beneath the cutting point is the highest, over 2000 MPa. Finally, the residual stresses from the surface to the depth of 0.2 mm are calculated. The point beneath the surface by 0.003 mm has the maximum residual stress. Then residual stress reduces to about zero at the point beneath the surface by 0.04 mm. The residual stress curve is plotted in Figure 4.3 with little squares in purple.

For comparison with the experiment and the FEA methods, Huang plotted the

residual stresses calculated with the methods in Figure 4.3. The results of Huang's and the experiment methods are close, and the result of the FEA method varies a lot from Huang's and the experimental methods.

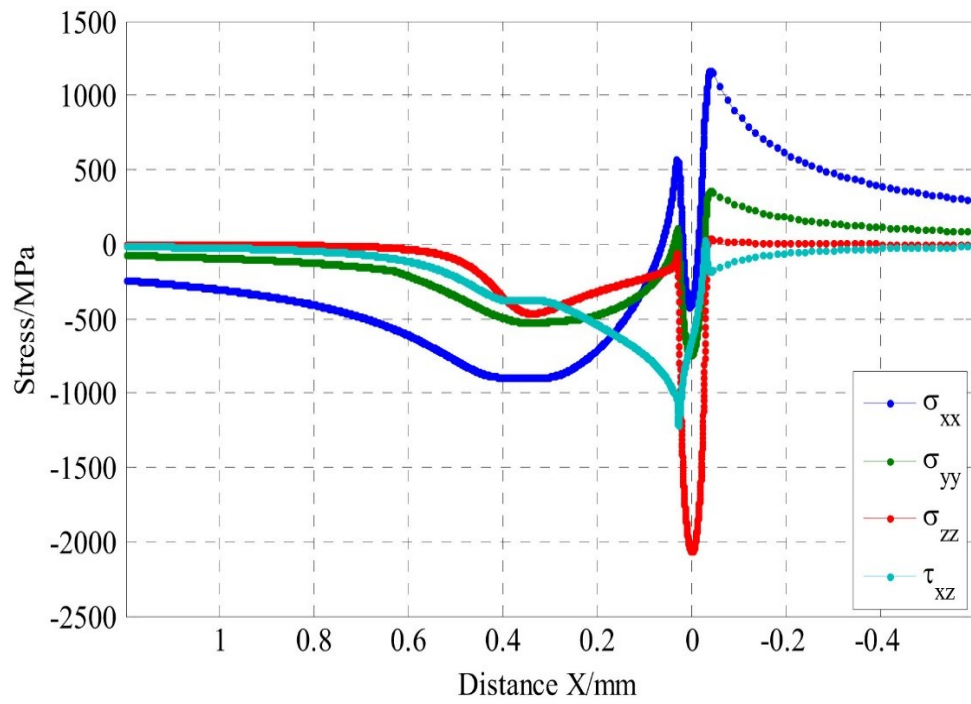


Figure 4.1 Stress history by Huang et al. (Z=3 μ m) [25]

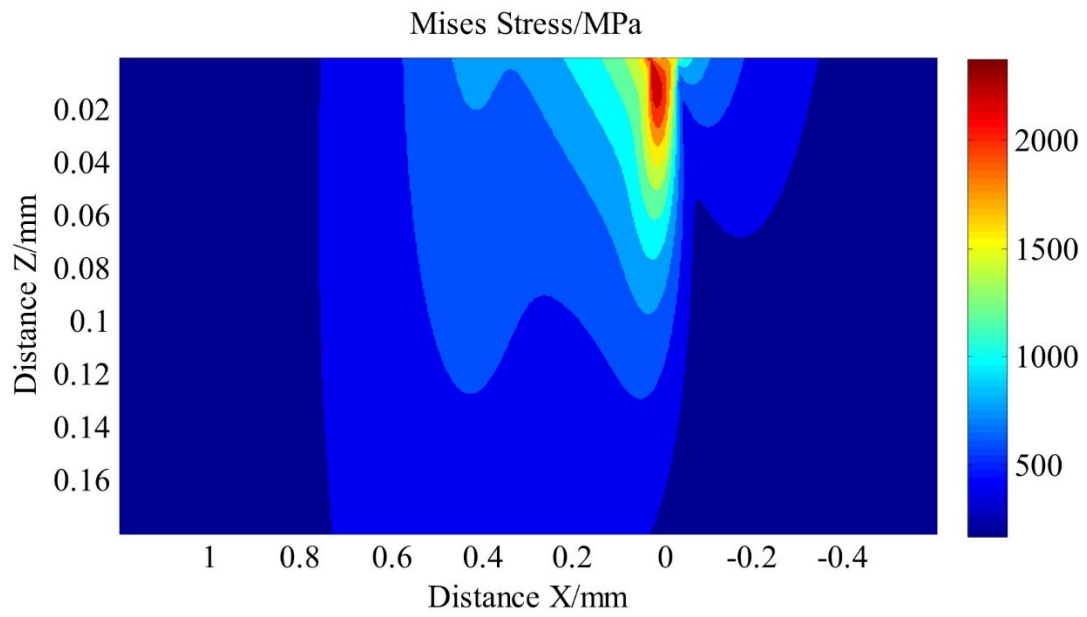


Figure 4.2 von Mises stress field by Huang et al. [25]

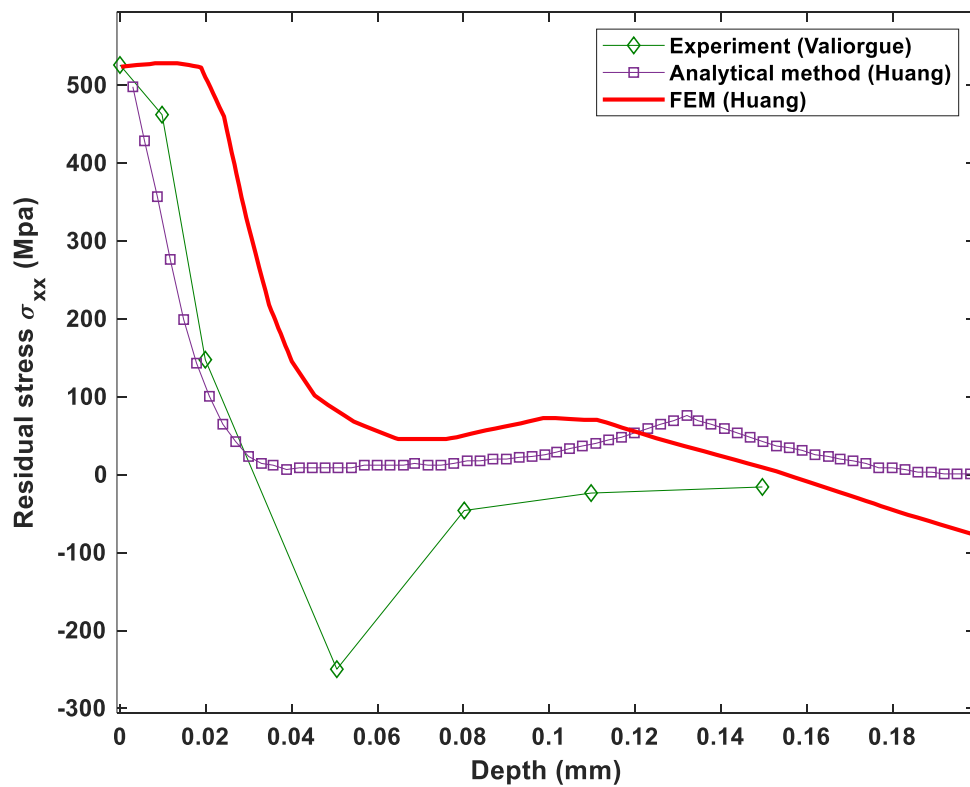


Figure 4.3 Comparison of residual stress [25]

4.1.2 Application of this proposed method to AISI 316L

To verify this newly proposed method, it is applied to AISI 316L under the same machining conditions as those in the published research. The reasons for this include (1) the example of machining AISI 316L is well established and recognized, and (2) due to the Covid 19 pandemic, the experiment of cutting AISI 316L cannot be conducted. In the thesis research, this new method has been implemented in a software of residual stress prediction with MATLAB. First, the above-mentioned cutting parameters are input into the software, the cutting stresses (σ_{xx} , σ_{yy} , σ_{zz} and σ_{xz}) in the range of the cutting point are calculated. This range is between the point in front of the cutting point by 1.2 mm and the point at the back of the cutting point by 0.6 mm. The cutting stresses are plotted in Figure 4.4.

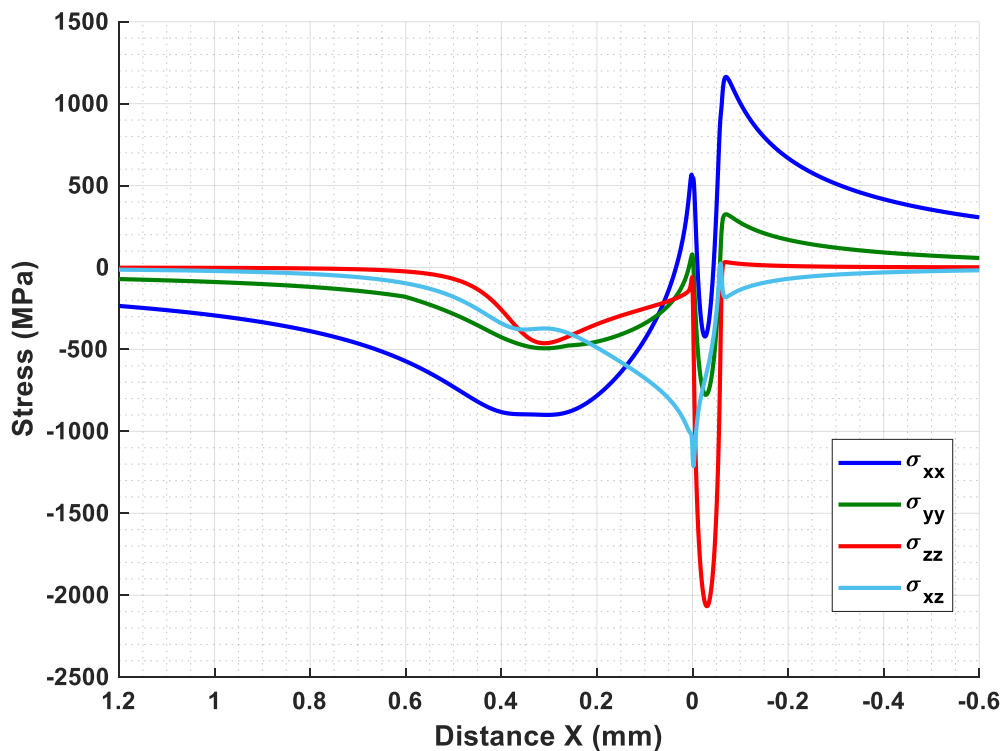


Figure 4.4 Stress history by the improved method ($Z=3\mu\text{m}$)

Then, the von Mises stress in the above range of the cutting point and to the

depth of 0.2 mm is calculated with the software. The von Mises stress distribution is plotted in Figure 4.5. It shows that the von Mises stress close the cutting point and beneath the surface by 0.008 mm is 2334 MPa, which is the maximum at the cutting moment. Finally, the residual stress from the surface to the depth of 0.2 mm is calculated with the software, and the residual stress curve is plotted in Figure 4.7 in blue.

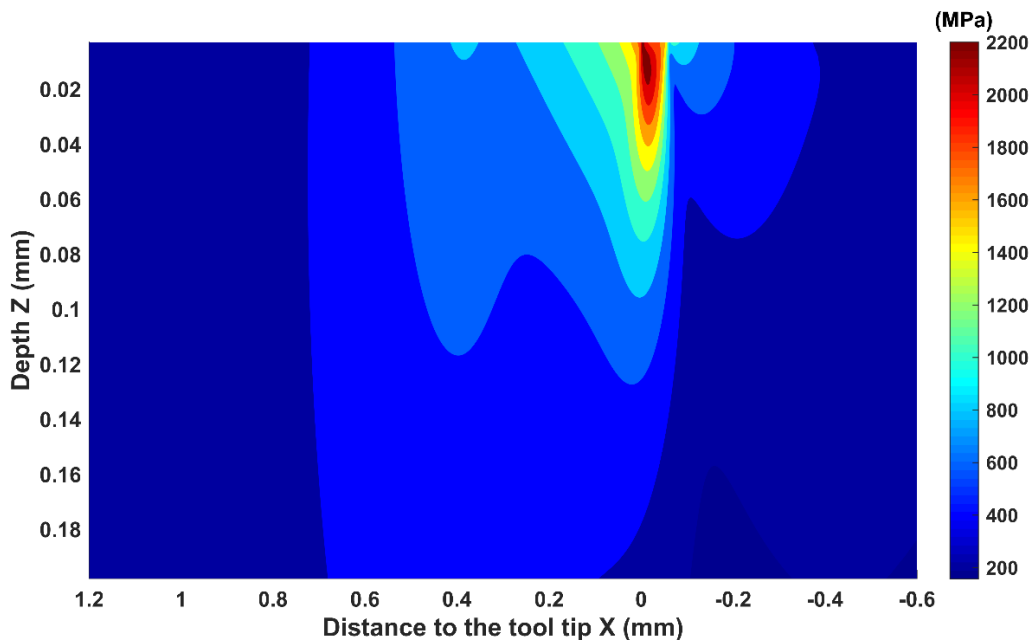


Figure 4.5 von Mises stress field by the improved method

To verify this new method the residual stress curve is plotted in the same figure (Figure 4.6). It is readily seen that the residual stresses calculated with the analytical methods are close to that of the experiment, while the result of the FEA method deviates much more from the experiment result. Residual stress on the machined surface tensile stress is valued at about 500 MPa and reduces in the surface and sub-surface layers. However, the residual stress in the surface layer (0 - 0.02 mm) affects the part deformation when residual stress releases. High residual tensile stress in the surface layer causes part fatigue failure and surface damage. Therefore, the residual stresses obtained by different methods in the surface layer are scrutinized, and they are zoomed in Figure 4.7. This figure shows that the residual stress curve of the

proposed method is accurate. Besides, the residual tensile stress in the surface layer calculated with the author's method is almost the same as the experiment result.

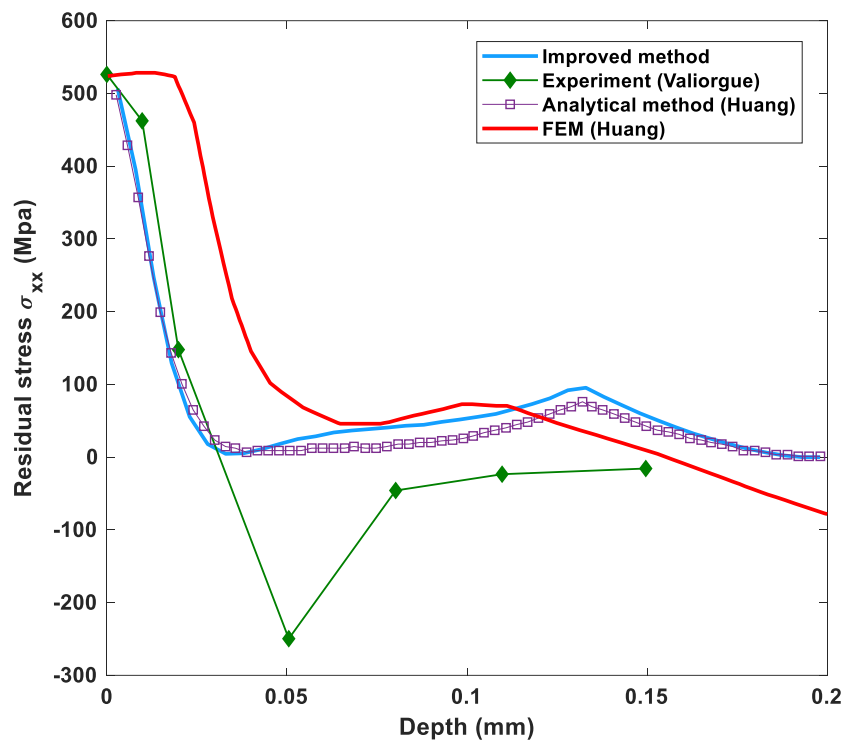


Figure 4.6 Comparison of residual stress

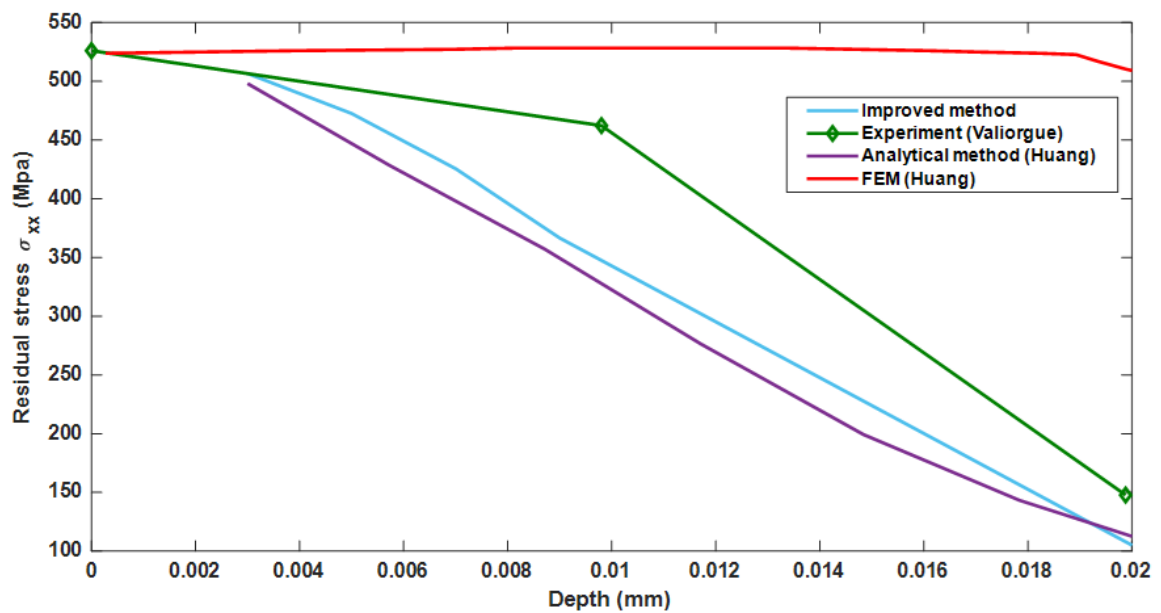


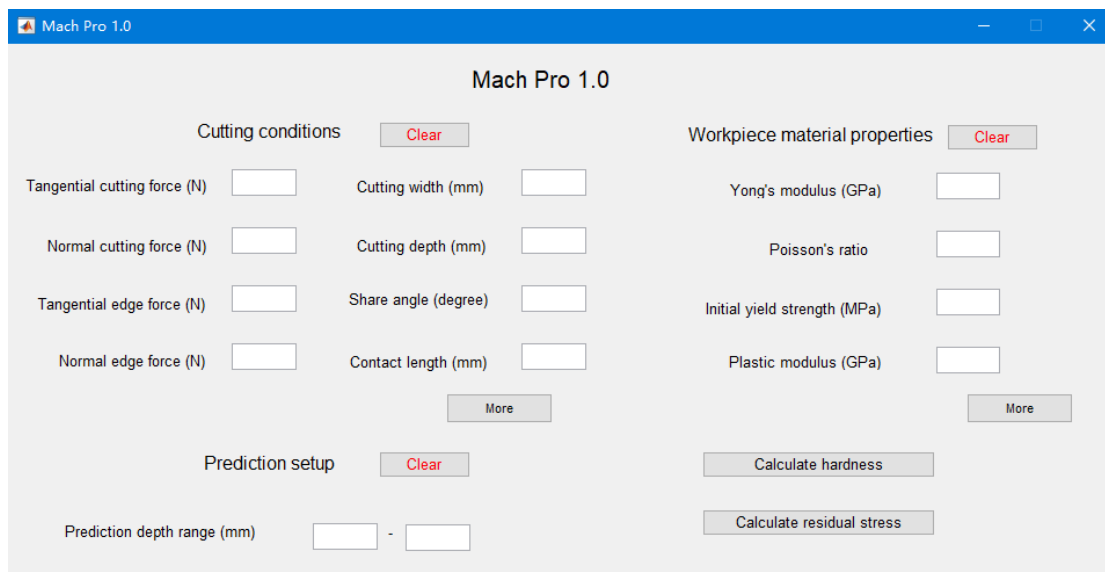
Figure 4.7 Residual stress of the surface layer

4.2 Application of the purposed method to Inconel 718

Since the proposed approach has been successfully applied to the conventional experiment of cutting AISI 316L, and the residual stress calculated with the proposed approach is accurate and efficient, it is more credential to apply them to cutting Inconel 718. The proposed approaches have been implemented in a software of hardness and residual stress prediction with MATLAB.

4.2.1 Cutting parameters optimization with the software

A software for hardness and residual stress prediction is developed with MATLAB and the main interface is shown in Figure 4.8. The main input parameters include cutting conditions and workpiece material properties. The depth range could be defined in the prediction setup.



The screenshot displays the 'Mach Pro 1.0' software interface. It is organized into three main sections: 'Cutting conditions', 'Workpiece material properties', and 'Prediction setup'. Each section has a 'Clear' button. The 'Cutting conditions' section includes input fields for Tangential cutting force (N), Normal cutting force (N), Tangential edge force (N), Normal edge force (N), Cutting width (mm), Cutting depth (mm), Share angle (degree), and Contact length (mm). The 'Workpiece material properties' section includes input fields for Yong's modulus (GPa), Poisson's ratio, Initial yield strength (MPa), and Plastic modulus (GPa). The 'Prediction setup' section includes a 'Prediction depth range (mm)' field with a range selector. There are also 'More' buttons for each section and 'Calculate hardness' and 'Calculate residual stress' buttons at the bottom right.

Figure 4.8 The interface of the software

With the prediction software, the cutting parameters can be optimized for less

residual stress and high cutting efficiency. First, calculate the residual stress generated in the multi-pass machining. Then check the part quality after the machining is finished. If the part is not qualified, modify the cutting parameters and repeat the prediction procedures; if the part is qualified, output the current cutting conditions as the optimal result. Figure 4.9 shows the main steps of the optimization.

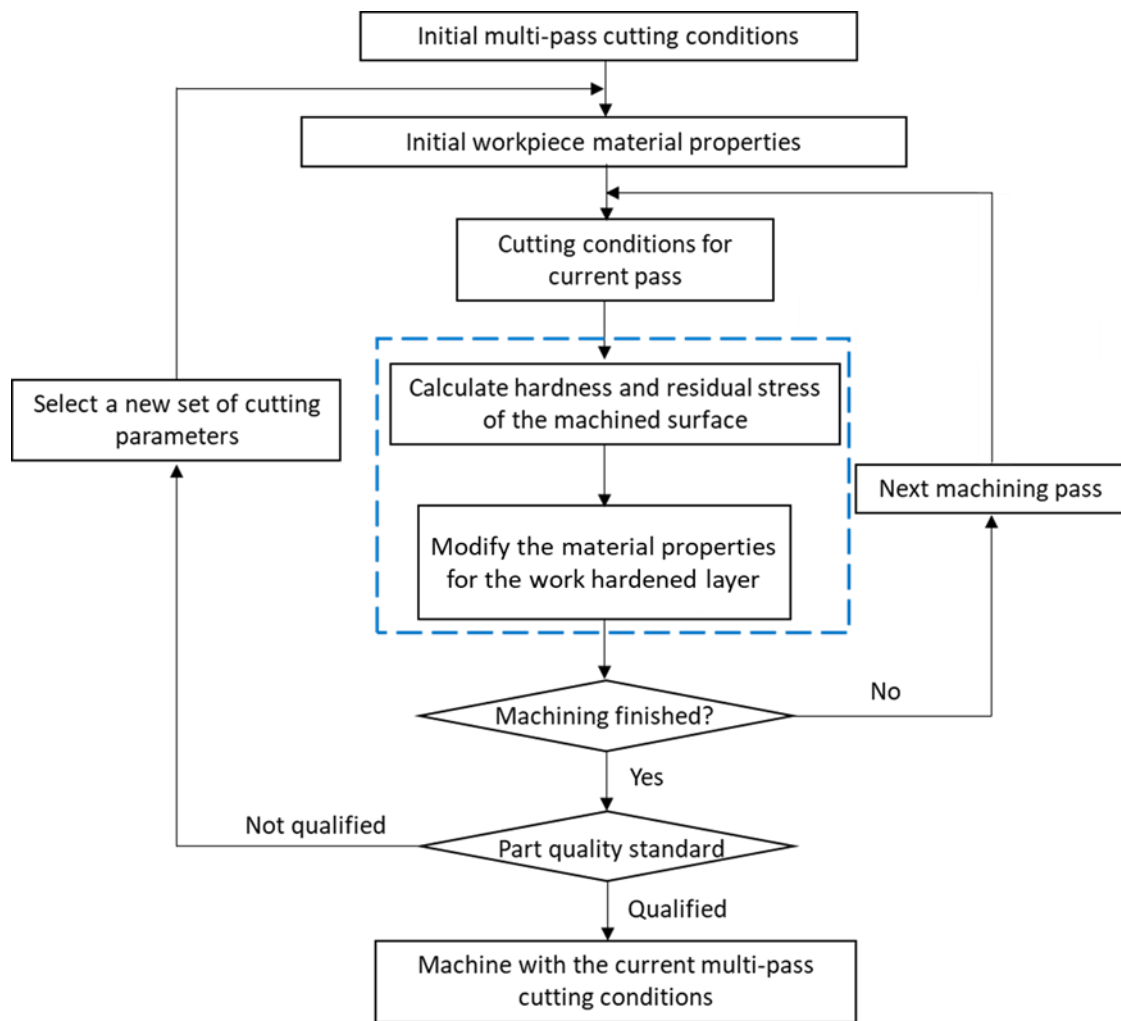


Figure 4.9 Cutting parameters optimization

4.2.2 Application of cutting parameters optimization

After the proposed method has been verified in the above section, it is applied to cutting Inconel 718. To demonstrate the procedure of the approach and the

robustness of the developed software, the new approach and the software have been applied to cutting Inconel 718 under two sets of cutting conditions. The cutting conditions are listed in Table 4.3. The details are provided in the following.

Table 4.3 Cutting conditions and measured variables for Inconel 718

Set	v (m/min)	t_1 (mm)	t_2 (mm)	F_c (N)	F_t (N)	ϕ (°)
1	20	0.2	0.350	1340.0	549.4	32.5207
2	30	0.2	0.346	1279.9	464.1	32.8631

An insert tool is employed for orthogonal cutting Inconel 718, and its inserts are coated carbide and the radii of the cutting edges are very small. The cutting parameters include the cutting width as 0.2 mm and the cutting depth as 0.35 mm. The cutting speed of the first is 20 m/min and the second set is 30 m/min. In cutting Inconel 718 with the above parameters, the cutting forces were measured with a Kistler dynamometer [65]. Since the radii of the cutting edges are very small, the cutting forces on the cutting edge contact area can be neglected and the resultant force of the measured cutting forces F_c and F_t equal to the resultant force acting on the shear plane.

The residual stresses (σ_{xx}^r and σ_{yy}^r) at the cutting point in the layer of 0.2 mm are calculated. The residual stress curves are plotted in Figure 4.10 and Figure 4.11. The high residual tensile stress in the tangential direction is mainly distributed in the surface layer and gradually decreases as the depth increases and becomes compressive at a depth of about 0.005 mm. Then a peak value of residual compressive stress appears at 0.025 mm. Compared with Set 1, Set 2 has a lower magnitude of residual tensile stress and a higher magnitude of residual compressive stress. Since the compressive residual stress is effective in improving fatigue performance, and tensile residual stress is detrimental to fatigue life, the residual stress result of Set 2 is

more conducive to the machined surface fatigue life than that of Set 1.

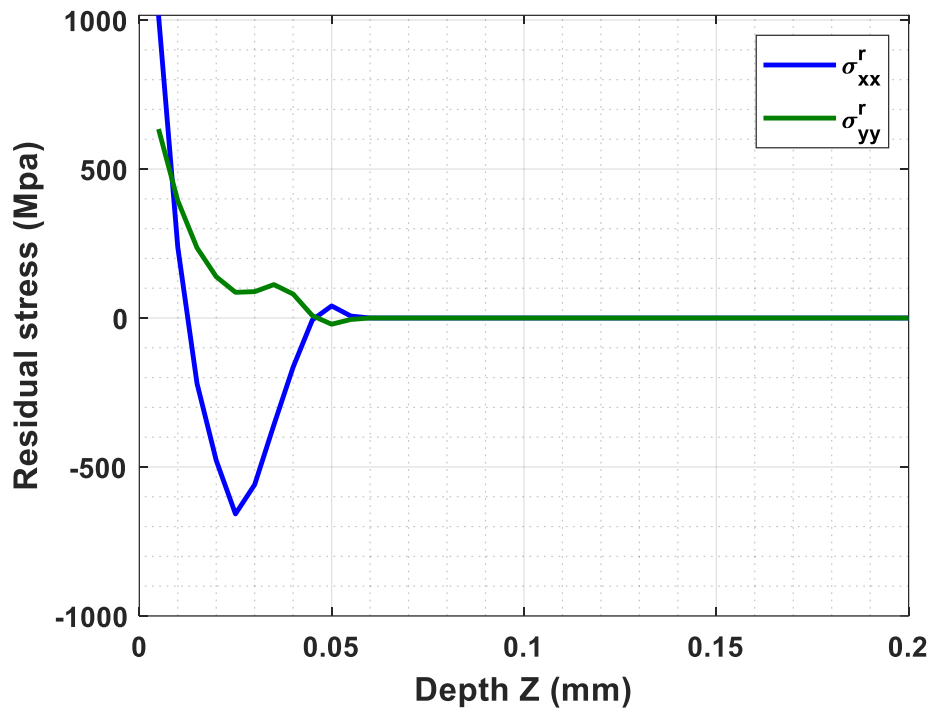


Figure 4.10 Residual stress of set 1

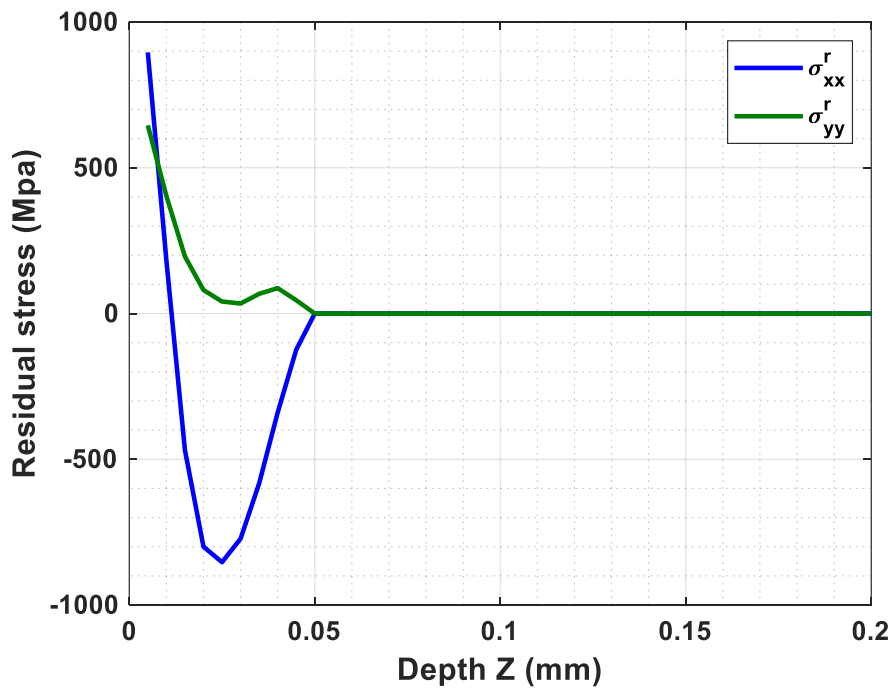


Figure 4.11 Residual stress of set 2

Another step of the optimization procedure is based on hardness. The hardness values of the work-hardened surface layer with a thickness of 0.2 mm of the two sets are calculated with the software. The parameter values are input into the software and the hardness curves are plotted in Figure 4.12 and Figure 4.13. The hardness of the work-hardened material in the depth of 0.005 mm is about 490 HV then decreases to 250 HV in the depth of 0.05 mm, and remains that value to the depth of 0.2 mm. It can be found that the hardness curves of the two sets are close in magnitude and depth, therefore the effects of work hardening on tool wear and machined surface quality of the two sets are also close. Compared with Set 1, the machined surface fatigue life of Set 2 is better and the tool wear rate is close. However, since the cutting speed of Set 1 is 20 m/min and the cutting speed of Set 2 is 30 m/min, the cutting efficiency of Set 2 is higher than set1. Therefore, the cutting parameters of Set 2 are better than Set 1 and should be employed in machining.

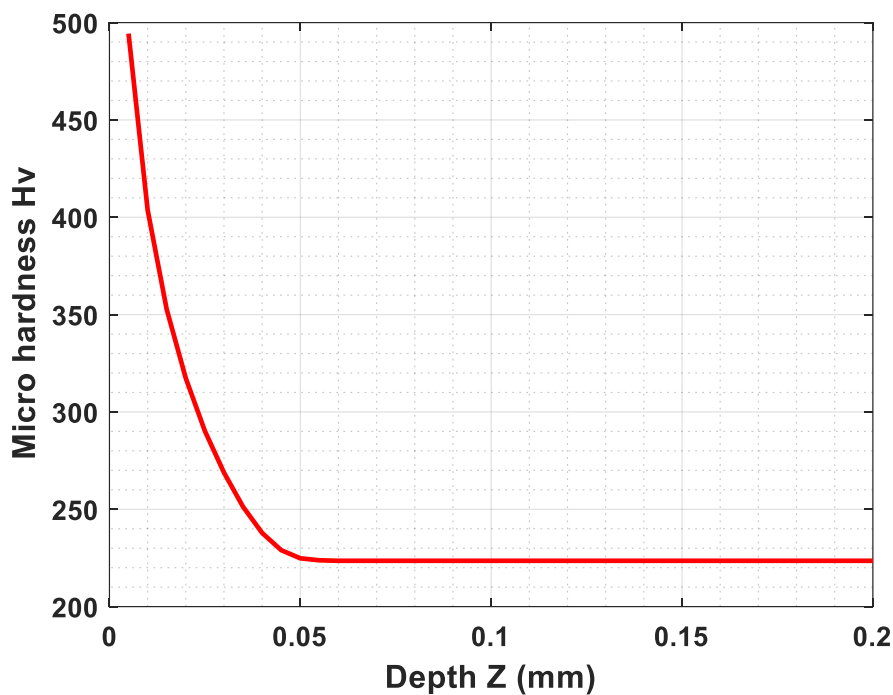


Figure 4.12 Microhardness of set 1

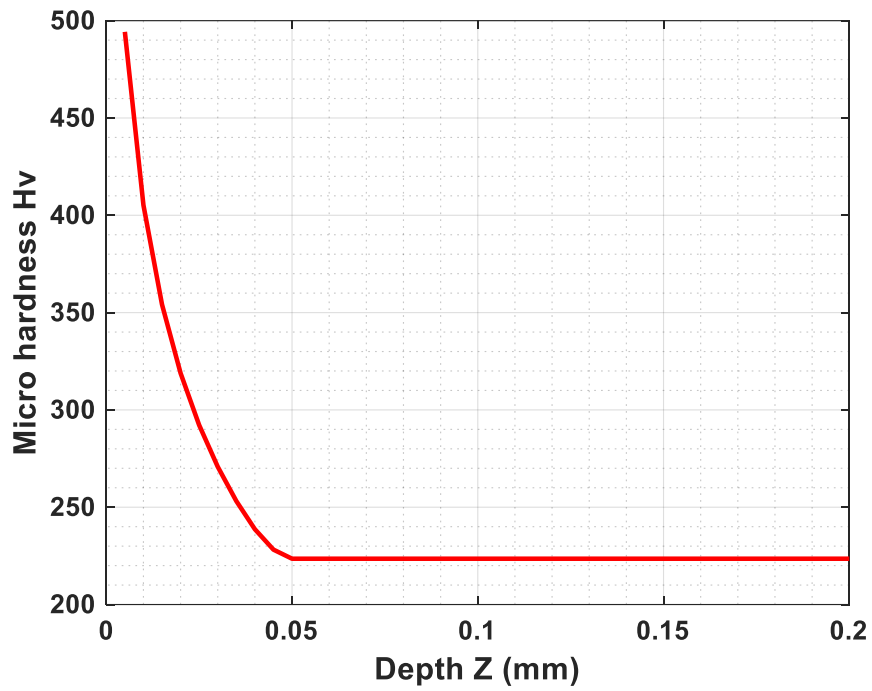


Figure 4.13 Microhardness of set 2

In this chapter, the proposed approach has been applied to a conventional experiment of cutting AISI 316L, and it has been verified. The proposed approach has also been applied to optimize the parameters of cutting Inconel 718. It has great potential to optimize the cutting parameters for less residual stress and high cutting efficiency.

CHAPTER 5 CONCLUSIONS AND FUTURE WORK

5.1 Conclusions

This research work has addressed the technical challenges of predicting work-hardening and residual stress in machining Inconel 718. In terms of work-hardening, a new analytical method of predicting the new hardness of the work-harden material on the machined surface has been built. This method has established the relationship of hardness and work hardening in machining Inconel 718. The hardness of the material beneath the machined surface is calculated from the stress experience. The advantages of this method include (1) compared to the existing finite element methods and experimental methods, this newly proposed method is analytical and is very efficient; and (2) this method can be used in Inconel 718 process planning to optimize the machining parameters.

Another outstanding achievement of this research is that an improved method of predicting residual stress in machining Inconel 718 parts is proposed. When predicting the stress and residual stress for the subsequent machining, the improved method considered the properties of the material, which is work-hardened in the prior machining. The advantage of this method includes that it helps control residual stresses within the surface of Inconel 718. This research has great potential to cut Inconel 718 with high machining efficiency and better part surface integrity.

5.2 Future work

This thesis research has proposed two methods of predicting the hardness and the residual stress of the hardened material on the machined surface. Due to the time

limit, the two methods have not been fully implemented in the process planning of machining Inconel 718. The newly proposed methods are essential to the process planning of machining Inconel 718. Besides, this thesis research is focused on the orthogonal cutting of Inconel 718, which is one type of machining. For another type of cutting, oblique cutting, the methods cannot be directly applied. In the future, the methods of predicting hardness and residual stress in oblique cutting Inconel 718 will be investigated.

BIBLIOGRAPHY

- [1] NASA, 12 Jun. 2014, Engines, YouTube,
<https://www.grc.nasa.gov/www/k12/UEET/StudentSite/engines.html>.
- [2] Pratt & Whitney, 18 Aug. 2017, How Jet Engines Work, YouTube,
https://www.youtube.com/watch?v=_LaKIE2h3Jw.
- [3] Mouritz P., 2012, Superalloys for Gas Turbine Engines, Introduction to Aerospace Materials, American Institute of Aeronautics and Astronautics, 2012, pp. 252.
- [4] Sourmail T., Coatings for Turbine Blades, Phase Transformations & Complex Properties Research Group,
<http://www.phasetrans.msm.cam.ac.uk/2003/Superalloys/coatings/index.html>.
- [5] Cervenka M., The Rolls-Royce Trent Engine, Phase Transformations & Complex Properties Research Group,
<https://www.phasetrans.msm.cam.ac.uk/mphil/Trent1/sld001.htm>.
- [6] Devillez A., Schneider F., Dominiak S., Dudzinski D., and Larrouquere D., 2007, Cutting Forces and Wear in Dry Machining of Inconel 718 with Coated Carbide Tools, *Wear*, vol. 262, no. 7, 2007, pp. 931–942.
- [7] Kitagawa T., Kubo A., and Maekawa K., 1997, Temperature and Wear of Cutting Tools in High-Speed Machining of Inconel 718 and Ti-6Al-6V-2Sn, *Wear*, vol. 202, no. 2, 1997, pp. 142–148.
- [8] Ezugwu E.O., Bonney J., and Yamane Y., 2003, An Overview of the Machinability of Aeroengine Alloys, *Journal of Materials Processing Technology*, vol. 134, no. 2, 2003, pp. 233–253.

- [9] TITANS of CNC: Academy, 10 Apr. 2020, YouTube, INCONEL 718 FAILED TEST-2nd Attempt | Ceramic End Mills & 1.5 HP TORMACH, <https://www.youtube.com/watch?v=VXaUl6of8m4>
- [10] Ezugwu E.O., Wang Z.M., and Machado A.R., 1999, The Machinability of Nickel-Based Alloys: A Review, *Journal of Materials Processing Technology*, vol. 86, no. 1-3, 1999, pp. 1–16.
- [11] Ren X., and Liu Z., 2016, Influence of Cutting Parameters on Work Hardening Behavior of Surface Layer during Turning Superalloy Inconel 718, *The International Journal of Advanced Manufacturing Technology*, vol. 86, no. 5-8, 2016, pp. 2319–2327.
- [12] Mahalle G., Omkar S., Kotkunde N., Gupta A.K., and Singh S.K., 2019, Neural Network Modeling for Anisotropic Mechanical Properties and Work Hardening Behavior of Inconel 718 Alloy at Elevated Temperatures, *Journal of Materials Research and Technology*, vol. 8, no. 2, 2019, pp. 2130–2140.
- [13] Liao Y.S., Lin H.M., and Wang J.H., 2008, Behaviors of End Milling Inconel 718 Superalloy by Cemented Carbide Tools, *Journal of Materials Processing Technology*, vol. 201, no. 1-3, 2008, pp. 460–465.
- [14] Sharman A.R.C., Hughes J.I., and Ridgway K., 2004, Workpiece Surface Integrity and Tool Life Issues When Turning Inconel 718™ Nickel Based Superalloy, *Machining Science and Technology*, vol. 8, no. 3, 2004, pp. 399–414.
- [15] Ma K., Goetz R., and Srivatsa S.K., 2010, Modeling of Residual Stress and Machining Distortion in Aerospace Components (preprint), Air Force Research Lab.
- [16] Griffiths B., 2001, *Manufacturing Surface Technology: Surface Integrity & Functional Performance*, Penton.

- [17] Matsumoto Y., Magda D., Hoepfner D.W., and Kim T.Y., 1991, Effect of Machining Processes on the Fatigue Strength of Hardened AISI 4340 Steel, *Journal of Manufacturing Science and Engineering*, vol. 113, no. 2, 1991, pp. 154–159.
- [18] Arunachalam R.M., Mannan M.A., and Spowageb A.C., 2004, Surface Integrity When Machining Age Hardened Inconel 718 with Coated Carbide Cutting Tools, *International Journal of Machine Tools and Manufacture*, vol. 44, no. 14, 2004, pp. 1481–1491.
- [19] Grzesik W., 2016, *Advanced Machining Processes of Metallic Materials*, 2nd Edition, Elsevier, 2016.
- [20] PCC Forged Products, SMC -HISTORY, http://www.pccforgedproducts.com/brands/special_metals/about_us/history.
- [21] SPECIAL METALS, INCONEL® alloy718, https://www.specialmetals.com/assets/smc/documents/inconel_alloy_718.pdf.
- [22] Beer F.P., Johnston E.R. Jr., DeWolf J.T., and Mazurek D.F., 2015, *Mechanics of Materials*. Seventh ed., McGraw-Hill Education, 2015.
- [23] Ranganath S., Guo C., and Holt S., 2009, Experimental Investigations Into the Carbide Cracking Phenomenon on Inconel 718 Superalloy Material, *ASME 2009 International Manufacturing Science and Engineering Conference*, vol. 2, 2009, pp. 33-39.
- [24] Aspinwall D.K, Dewes R.C., Ng E.G., Sage C., and Soo S.L., 2007, The Influence of Cutter Orientation and Workpiece Angle on Machinability When High-Speed Milling Inconel 718 Under Finishing Conditions, *International Journal of Machine Tools and Manufacture*, vol. 47, no. 12, 2007, pp. 1839–1846.

- [25] Huang X., Zhang X., and Ding H., 2016, A Novel Relaxation-Free Analytical Method for Prediction of Residual Stress Induced by Mechanical Load during Orthogonal Machining, *International Journal of Mechanical Sciences*, vol. 115-116, 2016, pp. 299–309.
- [26] Coelho R.T., Silva L.R., Braghini A. Jr., and Bezerra A.A., 2004, Some Effects of Cutting Edge Preparation and Geometric Modifications When Turning Inconel 718™ at High Cutting Speeds, *Journal of Materials Processing Technology*, vol. 148, no. 1, 2004, pp. 147–153.
- [27] Zhuang K., Zhu D., Zhang X., and Ding H., 2014, Notch Wear Prediction Model in Turning of Inconel 718 with Ceramic Tools Considering the Influence of Work Hardened Layer, *Wear*, vol. 313, no. 1-2, 2014, pp. 63–74.
- [28] Sharman A.R.C., Hughes J.I., and Ridgway K., 2006, An Analysis of the Residual Stresses Generated in Inconel 718™ When Turning, *Journal of Materials Processing Technology*, vol. 173, no. 3, 2006, pp. 359–367.
- [29] Pawade R.S., Joshi S., and Brahmankar P.K., 2008, Effect of Machining Parameters and Cutting Edge Geometry on Surface Integrity of High-Speed Turned Inconel 718, *International Journal of Machine Tools and Manufacture*, vol. 48, no. 1, 2008, pp. 15–28.
- [30] Ezugwu E.O., and Tang S.H., 1995, Surface Abuse When Machining Cast Iron (G-17) and Nickel-Base Superalloy (Inconel 718) with Ceramic Tools, *Journal of Materials Processing Technology*, vol. 55, no. 2, 1995, pp. 63-69.
- [31] Thakur D.G., Ramamoorthy B., and Vijayaraghavan L., 2012, Effect of Cutting Parameters on the Degree of Work Hardening and Tool Life during High-Speed Machining of Inconel 718, *The International Journal of Advanced Manufacturing Technology*, vol. 59, no. 5-8, 2012, pp. 483–489.

- [32] Rinaldi S., Imbrogno S., Rotella G., Umbrello D., and Filice L., 2019, Physics Based Modeling of Machining Inconel 718 to Predict Surface Integrity Modification, *Procedia Cirp*, vol. 82, 2019, pp. 350–355.
- [33] M'Saoubi R., Outeiro J.C., Changeux B., Lebrun J.L., and Dias A.M., 1999, Residual Stress Analysis in Orthogonal Machining of Standard and Resulfurized AISI 316L Steels, *Journal of Materials Processing Technology*, vol. 96, no. 1-3, 1999, pp. 225–233.
- [34] Lavella M., and Berruti T., 2009, The Residual Stress State Due to Machining of Turbine Components: Experimental Investigation. *Structural Durability & Health Monitoring*, vol. 5, no. 4, 2009, pp. 337–349.
- [35] Madariaga A., Kortabarria A., Hormaetxe E., Garay A., and Arrazola P.J., 2016, Influence of Tool Wear on Residual Stresses When Turning Inconel 718, *Procedia Cirp*, vol. 45, 2016, pp. 267–270.
- [36] Arunachalam R.M., Mannan M.A., and Spowage A.C., 2004, Residual Stress and Surface Roughness When Facing Age Hardened Inconel 718 with Cbn and Ceramic Cutting Tools, *International Journal of Machine Tools and Manufacture*, vol. 44, no. 9, 2004, pp. 879–887.
- [37] Pusavec F., Hamdi H., Kopac J., and Jawahir I.S., 2011, Surface Integrity in Cryogenic Machining of Nickel Based Alloy—Inconel 718, *Journal of Materials Processing Technology*, vol. 211, no. 4, 2011, pp. 773–783.
- [38] Hua Y., and Liu Z., 2018, Experimental Investigation of Principal Residual Stress and Fatigue Performance for Turned Nickel-Based Superalloy Inconel 718, *Materials*, vol. 11, no. 6, 2018, pp. 879–893.
- [39] Jacobus K., DeVor R.E., and Kapoor S.G., 2000, Machining-Induced Residual Stress: Experimentation and Modeling, *Journal of Manufacturing Science and Engineering*, vol. 122, no. 1, 2000, pp. 20–31.

- [40] Ulutan D., Alaca B.E., and Lazoglu I., 2007, Analytical Modelling of Residual Stresses in Machining, *Journal of Materials Processing Technology*, vol. 183, no. 1, 2007, pp. 77–87.
- [41] Jiang Y., and Sehitoglu H., 1994, An Analytical Approach to Elastic-Plastic Stress Analysis of Rolling Contact, *Journal of Tribology*, vol. 116, no. 3, 1994, pp. 577–587.
- [42] Liang S.Y., and Su J.C., 2007, Residual Stress Modeling in Orthogonal Machining, *Cirp Annals - Manufacturing Technology*, vol. 56, no. 1, 2007, pp. 65–68.
- [43] McDowell D.L., 1997, An Approximate Algorithm for Elastic-Plastic Two-Dimensional Rolling/Sliding Contact, *Wear*, vol. 211, no. 2, 1997, pp. 237–246.
- [44] Wan M., Ye X., Yang Y., and Zhang W., 2017, Theoretical Prediction of Machining-Induced Residual Stresses in Three-Dimensional Oblique Milling Processes, *International Journal of Mechanical Sciences*, vol. 133, 2017, pp. 426–437.
- [45] Huang, X., Zhang X., and Ding H., 2015, An Analytical Model of Residual Stress for Flank Milling of Ti-6Al-4V, *Procedia Cirp*, vol. 31, 2015, pp. 287–292.
- [46] Ji X., Li B.Z., and Liang S.Y., 2018, Analysis of Thermal and Mechanical Effects on Residual Stress in Minimum Quantity Lubrication (MQL) Machining, *Journal of Mechanics*, vol. 34, no. 1, 2018, pp. 41–46.
- [47] Lin Z.C., Lin Y.Y., and Liu C.R., 1991, Effect of Thermal Load and Mechanical Load on the Residual Stress of a Machined Workpiece, *International Journal of Mechanical Sciences*, vol. 33, no. 4, 1991, pp. 263–278.

- [48] Lo S.P., 2000, An Analysis of Cutting Under Different Rake Angles Using the Finite Element Method, *Journal of Materials Processing Technology*, vol. 105, no. 1, 2000, pp. 143–151.
- [49] Lin Z.C., Lai W.L., Lin H.Y., and Liu C.R., 2000, The Study of Ultra-Precision Machining and Residual Stress for NiP Alloy with Different Cutting Speeds and Depth of Cut, *Journal of Materials Processing Technology*, vol. 97, no. 1, 2000, pp. 200–210.
- [50] Sasahara H., Obikawa T., and Shirakashi T., 2004, Prediction Model of Surface Residual Stress Within a Machined Surface by Combining Two Orthogonal Plane Models, *International Journal of Machine Tools and Manufacture*, vol. 44, no. 7, 2004, pp. 815–822.
- [51] Umbrello D., Ambrogio G., Filice L., and Shivpuri R., 2008, A Hybrid Finite Element Method-Artificial Neural Network Approach for Predicting Residual Stresses and the Optimal Cutting Conditions during Hard Turning of AISI 52100 Bearing Steel, *Materials and Design*, vol. 29, no. 4, 2008, pp. 873–883.
- [52] Li B., Jiang X., Yang J., and Liang S.Y., 2015, Effects of Depth of Cut on the Redistribution of Residual Stress and Distortion during the Milling of Thin-Walled Part, *Journal of Materials Processing Technology*, vol. 216, 2015, pp. 223–233.
- [53] Yang D., Liu Z., Ren X., and Zhuang P., 2016, Hybrid Modeling with Finite Element and Statistical Methods for Residual Stress Prediction in Peripheral Milling of Titanium Alloy Ti-6Al-4V, *International Journal of Mechanical Sciences*, vol. 108-109, 2016, pp. 29–38.
- [54] Shaw M.C., 2005, *Metal Cutting Principles*. 2nd ed., Oxford University Press.
- [55] Su J.C., 2006, *Residual stress modeling in machining processes*, Georgia Institute of Technology.

- [56] Kistler Group, 2014, Cutting Force Measurement, Kistler Group.
- [57] Meyers M.A., and Chawla K.K., 2009, Mechanical Behavior of Materials, Cambridge University Press.
- [58] Zhuang Z., Liu Z., and Cui Y., 2019, Dislocation Mechanism-Based Crystal Plasticity: Theory and Computation at the Micron and Submicron Scale, Academic Press.
- [59] Callister W.D., and Rethwisch D.G., 2018, Materials Science and Engineering: An Introduction, 10th ed., Wiley.
- [60] Voyiadjis G.Z., and Yaghoobi M., 2019, Size Effects in Plasticity: from Macro to Nano, Academic Press.
- [61] Fionn D., and Petrinic N., 2005, Introduction to Computational Plasticity, Oxford University Press.
- [62] Konrad H., 2011, Hardness Testing: Principles and Applications, ASM International.
- [63] Withers P.J., and Bhadeshia H.K.D.H., 2001, Residual Stress. Part 1—Measurement Techniques, Materials Science and Technology, vol. 17, 2001, pp.355–365.
- [64] Ulutan D., and Ozel T., 2011, Machining Induced Surface Integrity in Titanium and Nickel Alloys: A Review, International Journal of Machine Tools and Manufacture, vol. 51, no. 3, 2011, pp. 250–280.
- [65] Zhou J., Ren J., Feng Y., Tian W., and Shi K., 2017, A modified parallel-sided shear zone model for determining material constitutive law, The International Journal of Advanced Manufacturing Technology, vol. 91, no. 1-4, 2017, pp. 589–603.